

Enhanced olivine dissolution in seawater through continuous grain collisions

Gunter Flipkens^{a,*}, Michael Fuhr^b, Géraldine Fiers^c, Filip J.R. Meysman^{d,e}, Raewyn M. Town^a, Ronny Blust^a

^a ECOSPHERE, Department of Biology, University of Antwerp, Antwerp, Belgium

^b GEOMAR Helmholtz Centre for Ocean Research Kiel, Kiel, Germany

^c PProGress, Department of Geology, Ghent University, Ghent, Belgium

^d Geobiology, Department of Biology, University of Antwerp, Antwerp, Belgium

^e Environmental Biotechnology, Department of Biotechnology, Delft University of Technology, Delft, the Netherlands

ARTICLE INFO

Associate editor: Alexis Navarre-Sitchler

Keywords:

Olivine
Ocean alkalization
Silicate weathering
Climate change mitigation

ABSTRACT

Carbon dioxide removal (CDR) technologies at a gigaton scale need to be developed and implemented within the next decades to keep global warming below 1.5 °C. Coastal enhanced silicate weathering is one of the proposed CDR techniques that aims to accelerate the natural process of CO₂-sequestration during marine chemical weathering of silicate minerals. To this end, finely ground rock containing olivine (Mg_xFe_{2-x}SiO₄) could be dispersed in dynamic coastal environments, where local biotic and abiotic factors potentially enhance the weathering process. However, accurate predictions of the olivine dissolution rate and the associated CO₂ sequestration under *in situ* conditions are currently lacking and ecosystem impacts remain to be assessed. Previously, it has been hypothesized that *in situ* grain collisions, induced by bed load transport due to currents and waves, could accelerate the *in situ* chemical weathering of olivine particles. To examine this, we investigated the effects of continuous grain tumbling on olivine dissolution in natural seawater. A 70-day experiment was conducted in which forsterite olivine sand was continuously tumbled in filtered seawater at different rotation speeds, and dissolution rates were measured on a weekly basis. Results showed that continuously tumbled olivine dissolved 8 to 19 times faster compared to stagnant (no rotation) conditions. Olivine dissolution was complete and stoichiometric (except for Ni release), air-seawater CO₂ exchange was not significantly rate limiting, and minimal particle fragmentation and secondary mineral formation were observed. Hence, we infer that olivine weathering was mainly enhanced via advective pore water flushing, which limits saturation effects at the grain scale. Overall, this study provides evidence that ambient physical stresses in coastal environments could enhance marine silicate weathering, which has implications for both the natural silicon cycle as well as the use of enhanced coastal weathering of silicates as a CDR technique.

1. Introduction

To constrain the adverse effects of climate change, the Paris Agreements foresee strong carbon dioxide (CO₂) emission cuts (UNFCC, 2015). Yet, such traditional mitigation in itself will not be enough, as climate stabilisation by 2100 also requires the implementation of active and large-scale carbon dioxide removal (CDR) from the atmosphere (Minx et al., 2018). A proposed technique for large-scale CDR is ocean alkalization via coastal enhanced silicate weathering (CESW) (Hangx and Spiers, 2009; Schuiling and De Boer, 2011; Meysman and

Montserrat, 2017; Minx et al., 2018). The underlying idea is that relatively coarsely ground particles (<150 μm grains) of suitable silicate rock are distributed in coastal environments, and that the local dynamics within these systems (including currents, waves, biota) help to speed up the process of natural chemical weathering (Meysman and Montserrat, 2017). During chemical weathering of a silicate mineral, alkalinity is released (i.e. protons are consumed), which drives additional transfer of atmospheric CO₂ to the surface ocean followed by storage as bicarbonate (HCO₃⁻) (Eq. (1) and (2) of Table 1) (Schuiling and Krijgsman, 2006; Meysman and Montserrat, 2017). Olivine (Mg_xFe_{2-x}SiO₄) has received

* Corresponding author.

E-mail address: Gunter.Flipkens@uantwerpen.be (G. Flipkens).

<https://doi.org/10.1016/j.gca.2023.09.002>

Received 4 February 2023; Accepted 5 September 2023

Available online 12 September 2023

0016-7037/© 2023 The Author(s). Published by Elsevier Ltd. This is an open access article under the CC BY license (<http://creativecommons.org/licenses/by/4.0/>).

Table 1

Chemical reactions relevant for enhanced olivine weathering in seawater. The olivine dissolution, seawater acid-base equilibrium, and possible secondary mineral formation reactions are shown.

Olivine dissolution	$Mg_xFe_{2-x}SiO_4 + 4H^+ \rightarrow xMg^{2+} + (2-x)Fe^{2+} + H_4SiO_4$	(1)
Seawater acid-base equilibrium	$CO_2(aq) + H_2O \rightleftharpoons HCO_3^- + H^+ \rightleftharpoons CO_3^{2-} + 2H^+$	(2)
Potential secondary mineral formation		
Aragonite/calcite	$Ca^{2+} + 2HCO_3^- \rightarrow CaCO_3 + CO_2 + H_2O$	(3)
Ferrous iron (Fe ²⁺) oxidation	$Fe^{2+} + 0.25O_2 + H^+ \rightarrow Fe^{3+} + 0.5H_2O$	(4)
Iron(III) hydroxide	$Fe^{3+} + 3H_2O \rightarrow Fe(OH)_3 + 3H^+$	(5)
Sepiolite	$2Mg^{2+} + 3H_4SiO_4 \rightarrow Mg_2Si_3O_7.5(OH)(H_2O)_3 + 4H^+ + 0.5H_2O$	(6)
Serpentine (chrysotile)	$3Mg^{2+} + 2H_4SiO_4 + H_2O \rightarrow Mg_3Si_2O_5(OH)_4 + 6H^+$	(7)
Talc	$3Mg^{2+} + 4H_4SiO_4 + 4H_2O \rightarrow Mg_3Si_4O_{10}(OH)_2 + 6H^+$	(8)

most attention for CESW application, as it is globally abundant and combines a relatively fast weathering rate with a theoretically high CO₂ sequestration potential (Schuiling and Krijgsman, 2006; Hangx and Spiers, 2009; Köhler et al., 2010; Schuiling and De Boer, 2011; Hartmann et al., 2013; Taylor et al., 2016; Meysman and Montserrat, 2017; Montserrat et al., 2017). However, before CESW can be utilised as a CDR approach, two main uncertainties remain to be addressed, namely environmental impacts and the effectiveness of CO₂ sequestration (Meysman and Montserrat, 2017).

Environmental impacts of coastal enhanced olivine weathering can be geophysical, chemical and biological in nature. From a chemical perspective, the seawater composition can change through addition of dissolved products released during olivine dissolution, including total alkalinity (TA), dissolved inorganic carbon (DIC), Mg, Si, Fe, and potentially toxic Ni and Cr (Montserrat et al., 2017; Flipkens et al., 2021). However, some of these components could be retained within the seafloor, and at present, little experimental data is available on weathering products released under actual *in situ* conditions. Currently, most studies on the environmental impacts of coastal enhanced olivine weathering have been solely computational (Köhler et al., 2013; Hauck et al., 2016; Taylor et al., 2016; Bach et al., 2019; Flipkens et al., 2021), and only a limited number of experimental studies are available, mainly focused on the effects of increased seawater TA and pH (Cripps et al., 2013; Albright et al., 2016; Gim et al., 2018; Gore et al., 2019; Ren et al., 2021; Ferderer et al., 2022; Guo et al., 2022).

The CO₂ sequestration rate of olivine (R_{CO_2}) describes the amount of CO₂ that is removed from the atmosphere during olivine dissolution within a given application area per unit time (e.g. $\mu\text{mol CO}_2$ per m² of application area per second). It can be written as:

$$R_{CO_2} = \gamma_{CO_2}^{net} R_i = \left[(\delta DIC / \delta TA)_{pCO_2} \alpha_{TA} 4(1 - \varepsilon) \right] [k_i A (1 - \Omega) C] \quad (9)$$

This expression features the net CO₂ sequestration efficiency $\gamma_{CO_2}^{net}$ ($\mu\text{mol CO}_2$ sequestered per μmol of olivine dissolved) and the olivine dissolution rate R_i (Meysman and Montserrat, 2017). The former describes the net amount of CO₂ that is sequestered upon dissolution of a given amount of olivine, and can be written as $\gamma_{CO_2}^{net} = (\delta DIC / \delta TA)_{pCO_2} \alpha_{TA} 4(1 - \varepsilon)$ (Moosdorf et al., 2014; Meysman and Montserrat, 2017; Fuhr et al., 2022). In this $(\delta DIC / \delta TA)_{pCO_2}$ represents the amount of atmospheric CO₂ sequestered upon the addition of 1 μmol of alkalinity to the coastal ocean ($\mu\text{mol DIC } \mu\text{mol}^{-1}$ TA). This thermodynamic quantity is dependent on the partial CO₂ pressure (pCO_2) in the atmosphere, and the salinity, temperature, and chemical composition of the local seawater (Hofmann et al., 2009). Likewise, the dimensionless factor α_{TA} accounts for the alkalinity released during olivine dissolution. In the idealized case, 4 μmol of alkalinity are released per μmol of olivine (Eqs. (1) and (9)), though in practice, dissolution may not be complete (e.g. providing serpentine rather than dissolved silicate) or secondary reactions may scavenge alkalinity (Fuhr et al., 2022). The factor α_{TA} accounts for this and ranges between 0 and 1, where the maximum value 1 is attained at complete olivine dissolution and no secondary reactions

removing alkalinity. The factor ε accounts for CO₂ emissions resulting from mining, grinding, and transportation (Moosdorf et al., 2014). The olivine dissolution rate R_i is in itself dependent on the olivine dissolution rate constant k_i ($\mu\text{mol olivine m}^{-2} \text{ s}^{-1}$), the reactive surface area A ($\text{m}^2 \text{ g}^{-1}$), the pore water saturation state Ω with respect to olivine, and the olivine loading C , which represents the amount of olivine per unit of area (g per m^2 of application area) (Eq. (9)) (Meysman and Montserrat, 2017). The olivine loading depends on the amount of source rock deployed per unit area and the silicate rock composition (i.e. the olivine content).

To properly assess the feasibility of coastal enhanced silicate weathering, all the factors featured in Eq. (9) should be properly constrained under realistic application conditions. Olivine dissolution rate constants have been extensively investigated under idealized laboratory conditions (i.e. $\alpha_{TA} = 1$ and $\Omega = 0$), as reviewed previously (Pokrovsky and Schott, 2000b; Hangx and Spiers, 2009; Rimstidt et al., 2012; Oelkers et al., 2018). The main factors influencing k_i are solution pH and temperature (Rimstidt et al., 2012; Oelkers et al., 2018). Note however that most data originate from laboratory experiments with idealized electrolyte solutions (e.g. NaCl solutions), rather than actual seawater. Currently, only three studies have investigated olivine dissolution in artificial or natural seawater (Montserrat et al., 2017; Rigopoulos et al., 2018; Fuhr et al., 2022).

Within actual CESW applications, olivine dissolution will occur on or in a coastal seabed, where biological and hydrodynamic processes could significantly affect olivine dissolution and associated CO₂ sequestration (Meysman and Montserrat, 2017). Overall, the effect of these natural biological and hydrodynamic processes on key parameters in Eq. (9), related to kinetics (k_i), effective alkalinity release (α_{TA}) and potential saturation effects (Ω), remain largely unexplored. Yet, this information is critically needed for relevant application conditions as to make accurate predictions on the CO₂ sequestration potential and environmental impacts of coastal enhanced olivine weathering (Meysman and Montserrat, 2017).

One important aspect is physical grain abrasion. In shallow marine systems, current and wave induced sediment saltation could potentially lead to significant grain abrasion and development of cracked surfaces (Schuiling and De Boer, 2011; Madhavaraju et al., 2021). This grain abrasion could prevent formation of cation depleted layers, which are known to slow down olivine dissolution (by decreasing k_i), or prevent secondary surface precipitates, which could scavenge alkalinity (by decreasing α_{TA}) (Meysman and Montserrat, 2017; Oelkers et al., 2018). Furthermore, grain fragmentation would increase the olivine surface area exposed to seawater (increasing A), and therefore enhance the olivine dissolution rate (see Eq. (9)) (Oelkers et al., 2018). Once olivine becomes mixed in the surface sediment, saturation affects which slow down olivine dissolution could be prevented by advective pore water flushing (decreasing Ω) (Schuiling and De Boer, 2011; Meysman and Montserrat, 2017). Finally, waves and currents are essential for ocean mixing (Bates et al., 2001), which is needed to transport CO₂ deficient (i.e. TA rich) bottom water to the ocean surface for atmospheric CO₂

uptake and equilibration (Bach et al., 2023). This CO₂ uptake constrains the seawater pH increase (and k_f decrease) as seen from Eq. (2).

Here, our aim was to investigate the effect of continuous grain collisions on the kinetics of olivine dissolution and metal ion release kinetics in natural seawater by conducting a long-term weathering experiment (70 days) with sequential sampling. We hypothesized that increased grain collisions would result in enhanced olivine dissolution, and so currents and waves could enhance olivine dissolution in CESW via grain abrasion induced during bedload transport.

2. Material and methods

2.1. Agitation experiments

A 70-day experiment was conducted, in which a mixture of dunite sand and natural seawater was continuously agitated in commercially available rotary tumblers (“Rock Tumbler”, Shandong Qiyang Tools Co.,

Ltd) (Fig. 1). The experiment was conducted in a darkened and temperature-controlled (15 °C) room under ambient pressure (~1 atm) and ambient CO₂ levels (~415 ppm). VANGUARD refractory grade dunite sand was obtained from the Sibelco mine in Åheim (Norway). This dunite sand is composed of 90.54 wt% olivine, of which 93.4% is forsterite (Mg₂SiO₄) and 6.6% is fayalite (Fe₂SiO₄) (Table 2; see supplementary section SI 1.1 and 1.2 for characterization procedure), and the experiments using this sand will be further referred to as “olivine treatments”. Natural seawater (salinity 33 ± 0.3‰) was collected two weeks prior to the start of the experiment from the North Sea coast (Sea Life Centre, Blankenberge, Belgium). Seawater was filtered through 0.2 µm pore-size cellulose acetate filters (OE66, Whatman) and stored in 20 L high density polyethylene (HDPE) containers in the dark at 15 °C until further use. Before experimental use, all equipment was immersed in 2 V/V% HCl (VWR International) for at least 24 h and subsequently thoroughly rinsed with ultrapure Milli-Q (MQ) water (Merck).

At the start of the experiment, HDPE bottles (2 L volume, Lamaplast,

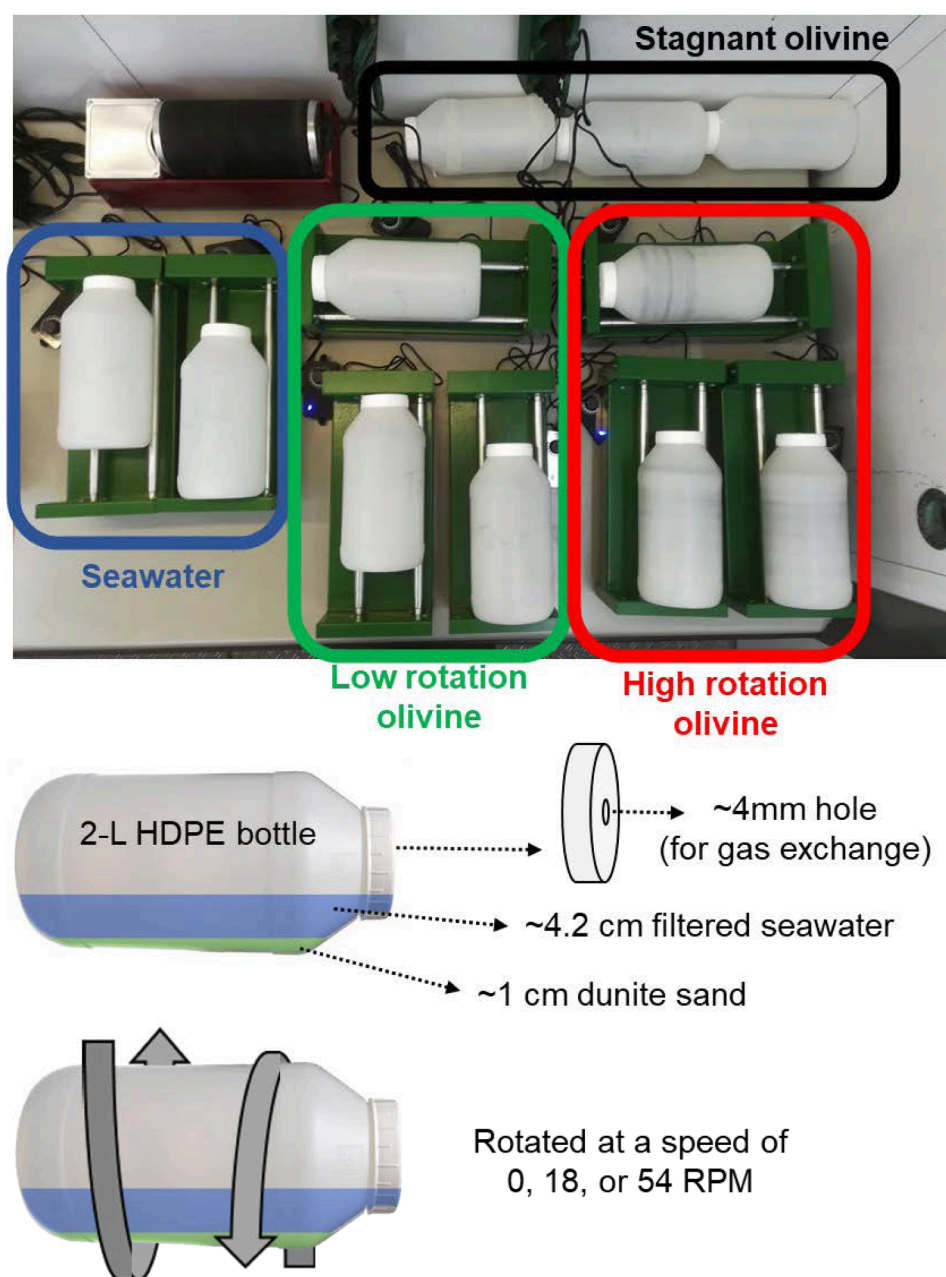


Fig. 1. Experimental set-up consisting of 11 bottles filled with a fixed amount of dunite sand and a fixed volume of filtered natural seawater. Bottles are rotated in commercial rock tumblers. Olivine treatments were conducted in triplicate and rotated at a rotation speed of 0 (stagnant), 18 (low rotation), or 54 (high rotation) rotations per minute (RPM). A seawater control without olivine was set up in duplicate and rotated at 54 RPM. A hole in the bottle cap allows gas exchange with the atmosphere during incubation.

Table 2

Characterization of the forsterite dunite sand used in the experiment. Mineral composition (based on TIMA high-resolution mapping), elemental composition (ICP-OES analysis), and textural composition, including grain size distribution (laser diffraction particle size analysis), specific surface area (geometric and Brunauer-Emmett-Teller (B.E.T.)), and mineral density are given. Details about the geochemical analyses of the olivine are given in supplementary section SI 1.1 and SI 1.2. Note that oxygen makes up the remaining approximately 44 wt% of the dunite elemental composition.

Mineral composition	Unit	Value
Olivine (Fo ₉₃)	wt%	90.54
Enstatite	“	6.02
Diopside	“	0.86
Clinocllore	“	0.85
Biotite	“	0.15
Pentlandite	“	0.05
Pyrope	“	0.02
Quartz	“	0.01
Others	“	1.48
Textural composition		
D10	µm	84 ± 1
D20	µm	99 ± 1
D50	µm	136 ± 1
D80	µm	186 ± 2
D90	µm	216 ± 2
Geometric specific surface area	m ² /g	0.0161 ± 0.002
B.E.T. specific surface area	m ² /g	0.9 ± 0.1
Mineral density	g cm ⁻³	3.3
Elemental composition		
Mg	wt%	30.4
Si	“	20.0
Fe	“	5.0
Cr	“	0.30
Ni	“	0.25
Al	“	0.081
Mn	“	0.068
K	“	0.025
Ca	“	0.018
Co	“	0.011
Ti	“	0.0060
Zn	“	0.0066

VWR International) were filled with a fixed mass of dunite sand (149.53 ± 0.01 g) and fixed amount of filtered natural seawater (718.2 ± 0.1 g or 700.0 ± 0.1 ml). This resulted in a ~ 1 cm of water-saturated sediment layer (~0.49 porosity) with a ~ 3.2 cm layer of overlying water on top (Fig. 1). This ~ 1 cm layer of mobile sediment mimics a rather intense bedload regime (Pruszek and Zeidler, 1994). Subsequently, bottles were inserted in the rock tumblers and rotated at a constant speed of 18 or 54 rotations per minute (RPM). This rotation speed falls within the range of natural gravity wave frequencies (2–60 waves per minute) (Toffoli and Bitner-Gregersen, 2017). These treatments will be respectively referred to as the “low rotation” and “high rotation” treatments. In addition, a “stagnant” treatment with olivine but no agitation (0 RPM) and a rotation treatment with only seawater (54 RPM; referred to as “seawater”) were used as controls. Olivine treatments were conducted in triplicate and the seawater control in duplicate. A small hole was made in the bottle cap to allow gas exchange with the atmosphere, so that O₂ and CO₂ concentrations could remain at atmospheric levels.

To determine the olivine dissolution rate as a function of time, consecutive accumulation sessions were performed, which each lasted one week. At the end of each session, water samples were taken from the overlying water of each bottle and the remaining water was replaced (so a new accumulation session could start). Water samples were analysed in duplicate for conductivity, pH, dissolved inorganic carbon (DIC), total alkalinity (TA), grain size distribution of suspended sediment, as well as dissolved metal concentrations. Additionally, sediment was collected at the start and end of the experiment to examine grain size distribution,

secondary mineral formation, grain surface dissolution features, and to quantify total extractable metal concentrations.

The weekly water sampling was conducted according to the following procedure. Immediately after removing the bottle from the rock tumblers, 50 ml of seawater was collected with a 20 ml syringe and filtered (0.2 µm pore size, Chromafil XTRA PES-20/25, Macherey-Nagel) for DIC analysis. This filtered seawater was stored in 50 ml Falcon tubes without headspace at 4 °C until further analysis within a week. Subsequently, the HDPE bottle was briefly put on a magnetic stirrer to create a homogeneous suspension. This was done to take standardized samples for the analysis of suspended sediment (and hence to verify whether abrasion led to small particle fragments). After allowing the majority of the sediment to settle for 20 s, either 140 or 220 ml (depending on the sample turbidity) of the supernatant was transferred to a 250 ml glass beaker. Water samples were always collected while the HDPE bottle was positioned on a balance (Sartorius CP4202S) to accurately determine the mass of seawater removal.

Subsequently, while stirring the supernatant solution in the glass beaker, a 40 ml sample was passed through a 0.2 µm pore size filter (OE66, Whatman) for dissolved metal analysis. Next, a volume of 20 ml or 100 ml (depending on the sample turbidity) of the unfiltered sample was collected for suspended sediment particle size analysis. Afterwards, the stirring was halted and the solution in the glass beaker was allowed to settle for 10 min before an unfiltered 20 ml seawater sample for pH and conductivity measurements was taken. Finally, the remaining 60 ml of seawater was filtered with 0.2 µm PES membrane filters and stored at 4 °C for TA analysis the subsequent day.

After sampling, the remaining seawater in the HDPE bottle (~400 ml) was gently removed with minimal loss of sediment (as discussed in supplementary section SI 2.6). The mass of the HDPE bottle was again determined to assess seawater removal. Subsequently, new filtered seawater was added to a total water volume of 700 ml, and HDPE bottles were put back onto the rock tumblers. This way, a new accumulation session could be started.

2.2. Geochemical solute analyses

Seawater salinity was determined using a CDC401 conductivity electrode coupled to a HQ30D portable multimeter (Hach). Calibration of the electrode was performed with a NIST conductivity standard (12880 µS/cm; VWR International) on each sampling day. pH was measured with a FiveEasy pH meter and LE438 pH electrode (Mettler Toledo). The pH electrode was calibrated before each use with three NIST buffers (pH 4.00, 7.00, and 10.01). Furthermore, pH of a TRIS (2-amino-2-hydroxy-1,3-propanediol) and AMP (2-aminopyridine) buffer, prepared according to the procedure by Dickson et al. (2007), were measured to convert pH data to the total hydrogen ion pH scale (Dickson et al., 2007).

The DIC concentration was determined with a Total Organic Carbon Analyzer (Shimadzu TOC-VCPH). For quality control, an ultrapure MQ water sample and 50 mg C/L TIC standard (Bernd Kraft) were included at the start and end of the analysis. The relative standard deviation (RSD) was better than 7.1% for all samples. Total alkalinity (TA) was analysed via an open cell potentiometric titration with 0.1 M HCl using an automated titrator setup (888 Titrandom, Metrohm). The TA was determined from the titrant volume and electromotive force measurement by the pH electrode using a non-linear least-squares method according to Dickson et al. (2007) with RSD values smaller than 1.6%.

Seawater samples for dissolved metal analysis were acidified with TraceMetal™ Grade 67–69% nitric acid (Fisher Scientific) to a final acid concentration of 1.4 V/V% and stored at –20 °C to minimize adsorption before further processing. Samples were diluted 20 times or 100 times (only for Na) with 3 V/V% HNO₃ to minimize matrix effects during analysis. Element concentrations were analysed by HR-ICP-MS (Element XR, Thermo Scientific). For quality control, NIST SRM 1640a certified reference samples (Merck) and procedural blanks (3 V/V% HNO₃) were

included in the analysis. A maximum RSD of 5% was allowed for the measurements.

2.3. Solid phase analysis

Grain size distribution was determined for the suspended sediment during weekly sampling (see Section 2.1) as well as for the bulk sediment at the start and end of the experiment. Suspended sediment was not pre-treated before analysis. Recovered bulk olivine sediment was gently rinsed with MQ water and dried at 60 °C for three days. Grain size distribution was determined with a laser diffraction particle size analyzer (Mastersizer 2000, Malvern Panalytical) according to standard operating procedures. Measurement RSD was lower than 16% for all grain size classes.

Total inorganic carbon (TIC) of 66 ± 9 mg fresh and weathered olivine samples was determined in triplicate with an elemental analyzer (Flash 2000 CN Soil Analyser, Interscience). Prior to analysis, samples were dried at 105 °C for 12 h and subsequently combusted in a muffle furnace at 375 °C for 17 h to remove the organic carbon (Wang et al., 2012). Since samples were homogeneous, no sample grinding was required. Results are expressed as a function of the sample dry weight.

2.4. Grain surface imaging

Grain morphology, magnesium to silicon (Mg/Si) ratios at the grain surface, and the presence of secondary minerals were investigated with a Phenom ProX scanning electron microscope (SEM) with energy dispersive spectrometer (EDS). To this end, dry olivine grains were fixed on aluminium (Al) pin stubs with double sided carbon tape. The atomic Mg and Si percentage was determined for 5 spots on the surface of 20 fresh and 10 weathered olivine grains with the accelerating voltage set to 15 kV. Microstructural changes and potential secondary mineral precipitation in the olivine grains were investigated using a Tescan MIRA3 SEM equipped with a Field Emission Gun (FEG) and EDS capability. Samples were fixed on an Al pin stub with double sided carbon tape to study surface features or embedded in an epoxy resin (EpoFix Resin and EpoFix Hardener, Struers), polished and carbon coated to study cross sections. For polishing, sand wetted with deionized (DI) water was first ground by hand on silicon carbide grinding paper (grit 500, 1000 and 2400) and subsequently polished on polishing cloths with Tegramin (Struers) using a diamond solution (DiaDuo-2, 6 µm, 3 µm, and 1 µm, Struers). Polished sand was rinsed with DI water and dried before analysis. The polished cross sections allow for investigating microstructural changes inside an olivine grain.

2.5. Olivine dissolution and CO₂ sequestration rate calculations

Olivine dissolution was tracked in weekly accumulation sessions, during which weathering products could accumulate in the overlying seawater. Concentrations of specific compounds C_i^k (µmol/L, with $i = \text{TA, DIC, DSi, DNi}$) were measured at the end time point t_k of each session k ($C_i^k = C_i(t_k)$) and are provided in the [supplementary Excel file](#). The accumulation ΔN_i^k (expressed in µmol) of a given compound i within a given session k is given by the mass balance expression

$$\Delta N_i^k = V_{\text{OW}}(t_{k-1})(C_i(t_k) - C_i^{\text{ASW control}}(t_k)) + V_{\text{PW}}(t_{k-1})(C_i(t_k) - C_i(t_{k-1})) \quad (10)$$

Here we assume that during water renewal, the pore water retains the concentration from the previous session $C_i(t_{k-1})$, while the overlying water is replaced with new stock solution. Furthermore, $C_i^{\text{ASW control}}(t_k)$ represents the concentration in the seawater control at timepoint t_k . The quantity $V_{\text{OW}}(t_{k-1})$ represents the volume (expressed in L) of stock seawater solution added at the start of a new session and is determined from the added seawater mass m_{OW} and the seawater density ρ_{SW} ($V_{\text{OW}} = m_{\text{OW}}/\rho_{\text{SW}}$). The volume of pore water that remained in the

sediment $V_{\text{PW}}(t_{k-1})$ was calculated from the mass of the filled (m_{BF}) and empty (m_{BE}) bottle, the initially added olivine mass (m_{olivine}), and the seawater density according to

$$V_{\text{PW}}(t_{k-1}) = \frac{m_{\text{BF}}(t_{k-1}) - m_{\text{BE}} - m_{\text{olivine}}}{\rho_{\text{SW}}} \quad (11)$$

The accumulation ΔN_i^k was subsequently normalized to the molar amount of olivine via

$$\Delta \hat{N}_i^k = \frac{\Delta N_i^k}{\frac{m_{\text{dunite}} \phi_{\text{olivine}}}{M_{\text{olivine}}}} \quad (12)$$

where $\Delta \hat{N}_i^k$ is the normalized accumulation (µmol/mol olivine), m_{dunite} the mass of dunite sand (expressed in g), ϕ_{olivine} its olivine fraction (0.9054, Table 2), and M_{olivine} the molar mass of the Fo₉₃ olivine ($M_{\text{olivine}} = 144.88 \text{ g mol}^{-1}$).

The pH excursion $\Delta pH(t_k)$ is defined as the pH difference with reference to the pH of the added seawater pH_{SW}

$$\Delta pH(t_k) = pH(t_k) - pH_{\text{SW}} \quad (13)$$

Using expression (10), we can calculate the compound specific olivine dissolution rate (expressed in µmol of olivine s⁻¹) via

$$R_i(t_k) = \frac{\Delta \hat{N}_i^k}{\nu_i(t_k - t_{k-1})} \quad (14)$$

where ν_i represents the theoretical stoichiometric coefficient (expressed in µmol/µmol olivine) for the specific compound in the olivine sand that we used ($\nu_{\text{TA}} = 3.73$, $\nu_{\text{DIC}} = 3.06$, $\nu_{\text{DSi}} = 1$, and $\nu_{\text{DNi}} = 0.0061$; Section SI 1.2 provides details on the derivation of these stoichiometric coefficients). The session time ($t_k - t_{k-1}$) was equal to 7 days (604800 s). In general, the olivine dissolution rate can be described by the kinetic rate expression

$$R_i(t_k) = m_{\text{olivine}} k_i(t_k) A(t_k) (1 - \Omega(t_k)) \quad (15)$$

In this, m_{olivine} represents the initial mass of olivine derived from the mass of dunite sand and its olivine fraction ($m_{\text{olivine}} = m_{\text{dunite}} \phi_{\text{olivine}}$), $k_i(t_k)$ is the dissolution rate constant (µmol olivine m⁻² s⁻¹), A is the specific surface area of the mineral grains (m²/g) and $\Omega(t_k)$ is the mineral saturation state (dimensionless). Using Eq. (15), we calculated k_i values from R_i values, assuming that solutions were always far from equilibrium ($\Omega(t_k) \ll 1$) and using the geometric surface area A_{GEO} (0.0161 m²/g) of fresh olivine as calculated from the measured grain size distribution (see [supplementary section SI 1.4](#)). Experimentally determined k_i values were compared to those predicted by the empirical rate expression for the olivine dissolution rate constant (mol m⁻² s⁻¹) given by [Rimstidt et al. \(2012\)](#)

$$k_{\text{olivine}} = 10^{4.07 - 0.256pH(t) - \frac{3465}{T}} \quad (16)$$

In which $pH(t)$ is the pH of the environment at a given time and T is the temperature (expressed in K).

The CO₂ sequestration rate (expressed in µmol CO₂ d⁻¹) can be calculated from the alkalinity release rate via

$$R_{\text{CO}_2} = \gamma_{\text{CO}_2} R_{\text{TA}} \quad (17)$$

In this, γ_{CO_2} denotes the CO₂ sequestration efficiency, i.e., the molar amount of CO₂ sequestered (expressed in µmol) per µmol of TA released during olivine dissolution. The CO₂ sequestration efficiency can be directly derived from the accumulation data of DIC and TA as

$$\gamma_{\text{CO}_2} = \Delta N_{\text{DIC}}^k / \Delta N_{\text{TA}}^k \quad (18)$$

For comparison, the CO₂ sequestration efficiency was also theoretically calculated from the applicable carbonate system relation in seawater, i.e. as $\gamma_{\text{CO}_2} = (\partial \text{DIC} / \partial \text{TA})_{p\text{CO}_2=420\text{ppm}}$ at the incubation temperature (15 °C) and salinity (33‰) using the R package AquaEnv

(Hofmann et al., 2010).

Finally, the seawater $p\text{CO}_2$ values were calculated using the carb function of the seacarb package in R with measured seawater pH and TA as input values. Additionally, seawater salinity, temperature, hydrostatic pressure (0 bar), and dissolved Si concentrations were taken into account and other settings were kept default.

2.6. Saturation state calculations

For a given mineral, the saturation state Ω is the ratio of the actual ion activity product and the solubility product. Mineral $\Omega(t_k)$ values were calculated in PHREEQC Interactive (version 3.7.3-15968) using the thermodynamic data from the LLNL database (Parkhurst and Appelo, 2013). The saturation index was subsequently calculated as $SI(t_k) = \log_{10}(\Omega(t_k))$ (undersaturation occurs at $SI(t_k) < 0$, supersaturation at $SI(t_k) > 0$). Weekly measured values of seawater temperature, TA, pH, and concentrations of major (Cl, Na, Mg, SO_4 , K, Ca) and minor and trace elements (Ni, Cr, Mn, Fe, Cu, Zn, Pb, Cd, Si) were used as input data for the calculation of $\Omega(t_k)$. Concentrations of Cl and SO_4 were not analytically determined but derived from the chemical composition of natural seawater (fixed ratio with measured Na concentrations) (Hem, 1985).

2.7. Modelling olivine dissolution and secondary mineral formation

Rates of olivine dissolution and secondary mineral precipitation were modelled with Wolfram Mathematica using the kinetic box model presented by Fuhr et al. (2022). This model implements olivine dissolution via the rate equation provided by Rimstidt et al. (2012), and accounts for precipitation of the secondary phases aragonite/calcite, sepiolite, chrysotile, talc and $\text{Fe}(\text{OH})_3$ through saturation state calculations. The model was adapted to the current conditions accounting for the rock water ratio, flask and sample volumes used in the experimental set-up.

The exchange of the entire water volume after each accumulation session may have led to the removal of small colloids, thus diminishing the available nuclei for formation of secondary mineral phases. For secondary precipitation reactions, the pre-factor $\varepsilon_{\text{pre}i}$ that defines when and how fast precipitation of mineral i starts in Eq. (3) by Fuhr et al. (2022) was changed to:

$$\varepsilon_{\text{pre}i} = k_{\text{pre}i} \left(1 - \frac{1}{1 + e^{\frac{-t}{\beta_i}}} \right) (2^{-k_2 \text{pre}i t}) \quad (19)$$

where $k_{\text{pre}i}$ is a kinetic rate constant, α_i defines the time delay of the precipitation and β_i steers the speed of the precipitation reaction. The tuning variable $k_2 \text{pre}i$ was added to the original Eq. (4) by Fuhr et al. (2022) to simulate a decrease in precipitation rates which can occur after the exchange of the water volume. Thus, with the combination of the two terms the model can simulate secondary mineral precipitation over a certain period of time. The other equations were used as in the original (see Fuhr et al. (2022) and supplementary section SI 1.6 for details). The constants used for the model calculations are listed in Supplementary Table S6.

2.8. Statistical analyses

All data are reported as mean and range values. Figures were constructed in GraphPad Prism version 9.4.0 for Windows. Statistical analyses were conducted in RStudio (version 1.2.5001) using R version 4.2.1 (R Core Team, 2022). To avoid the assumption of normally distributed data based on few replicate measurements, a non-parametric Kruskal-Wallis ANOVA was used to investigate differences in Mg/Si ratio, A_{GEO} , TIC, and olivine weight loss among treatments. Equal variance of residuals (i.e. homoscedasticity) was assessed visually with residual plots and statistically with Levene's test. Post hoc multiple

comparisons were performed with the Dunn's multiple comparisons test. Adjustment of p-values was done using Benjamini-Hochberg's method. Results were considered statistically significant when p-value < 0.05 .

3. Results

3.1. Olivine dissolution in seawater under agitated conditions

Our results show a clear impact of continuous tumbling on the olivine dissolution rate, as shown by the accumulation of the two main weathering products DSi and TA (Fig. 2). In the stagnant treatment, significant DSi and TA accumulations were only observed during the first week (Fig. 2A and C). In contrast, weekly accumulation values $\Delta \hat{N}_i^k$ for DSi and TA were significantly higher in the rotation treatments compared to the stagnant treatment on most sampling days (Fig. 2A–D). At day 70, cumulative TA accumulation was respectively 5.3 and 6.8 times higher in the low and high rotation treatment compared to the stagnant treatment (Fig. 2B). Similarly, continuous rotation enhanced DSi accumulation by a factor of 4 to 5.6 compared to stagnant conditions (Fig. 2D).

The olivine dissolution rate showed a marked dependence on time. Immediately after adding seawater to olivine, we already observed a notable increase in DSi and TA (Fig. 2A and C). Moreover, at the first consecutive sampling point (day 7), accumulations of TA and DSi were considerably higher compared to most other sampling days (Fig. 2A and C). After two weeks, TA and DSi accumulations remained relatively constant in time in the low rotation treatment (Fig. 2A and C), thus providing linear cumulative curves (Fig. 2B and D). In the high rotation treatment, there was a decreasing trend in TA and DSi accumulations (Fig. 2A and C), which resulted in a flattening of the cumulative curve near the end of the experiment (Fig. 2B, D). Negative accumulation values are the result of uncertain pore water reaction product concentrations (Eq. (10)) and possible phyllosilicate formation (Section 3.2).

DSi and TA accumulations were strongly correlated, thus suggesting stoichiometric olivine dissolution (Fig. 2E). Theoretically, 4 mol of TA and 1 mol of DSi should accumulate upon complete dissolution of 1 mol of forsterite olivine in the absence of secondary mineral formation (Table 1). However, in addition to Mg-bearing forsterite, olivine contains a fraction of Fe-bearing fayalite (here 6.6%). Under oxic conditions, the Fe^{2+} released during dissolution of fayalite will be oxidized, which reduces the TA/DSi release ratio to 3.73 for the experimental olivine (dashed line in Fig. 2E; supplementary section SI 1.2). While there is some variability, this expected relationship compares well with the experimentally observed TA/DSi ratio (slope = 3.43), thus suggesting stoichiometric olivine dissolution for TA and DSi.

3.2. Potential of secondary mineral formation

The pH response is fully in line with the expected response of the seawater carbonate system towards TA changes (i.e. higher TA induces higher pH at constant $p\text{CO}_2$). Immediately after olivine addition, the pH of the overlying seawater became significantly elevated ($\Delta \text{pH}(t_k = 0) = 0.19\text{--}0.24$) in all olivine treatments compared to the seawater control (Fig. 3A). At subsequent sampling times, the observed pH excursion $\Delta \text{pH}(t_k)$ gradually decreased in the stagnant treatment (Fig. 3A). For the low rotation treatment, $\Delta \text{pH}(t_k)$ varied between 0.14 and 0.39 with peak values on day 7 and day 63. For the high rotation treatment, $\Delta \text{pH}(t_k)$ varied between 0.09 and 0.35, and showed a peak value on day 7 and a decreasing trend on later sampling days (Fig. 3A).

Changes in seawater chemistry during olivine dissolution can alter saturation indices of various mineral phases (e.g. aragonite and phyllosilicates) (Griffioen, 2017; Fuhr et al., 2022). The aragonite $SI(t_k)$ was positive for all treatments throughout the experiment (Fig. 3B). Little variation in aragonite SI was observed in the seawater control ($SI(t_k) =$

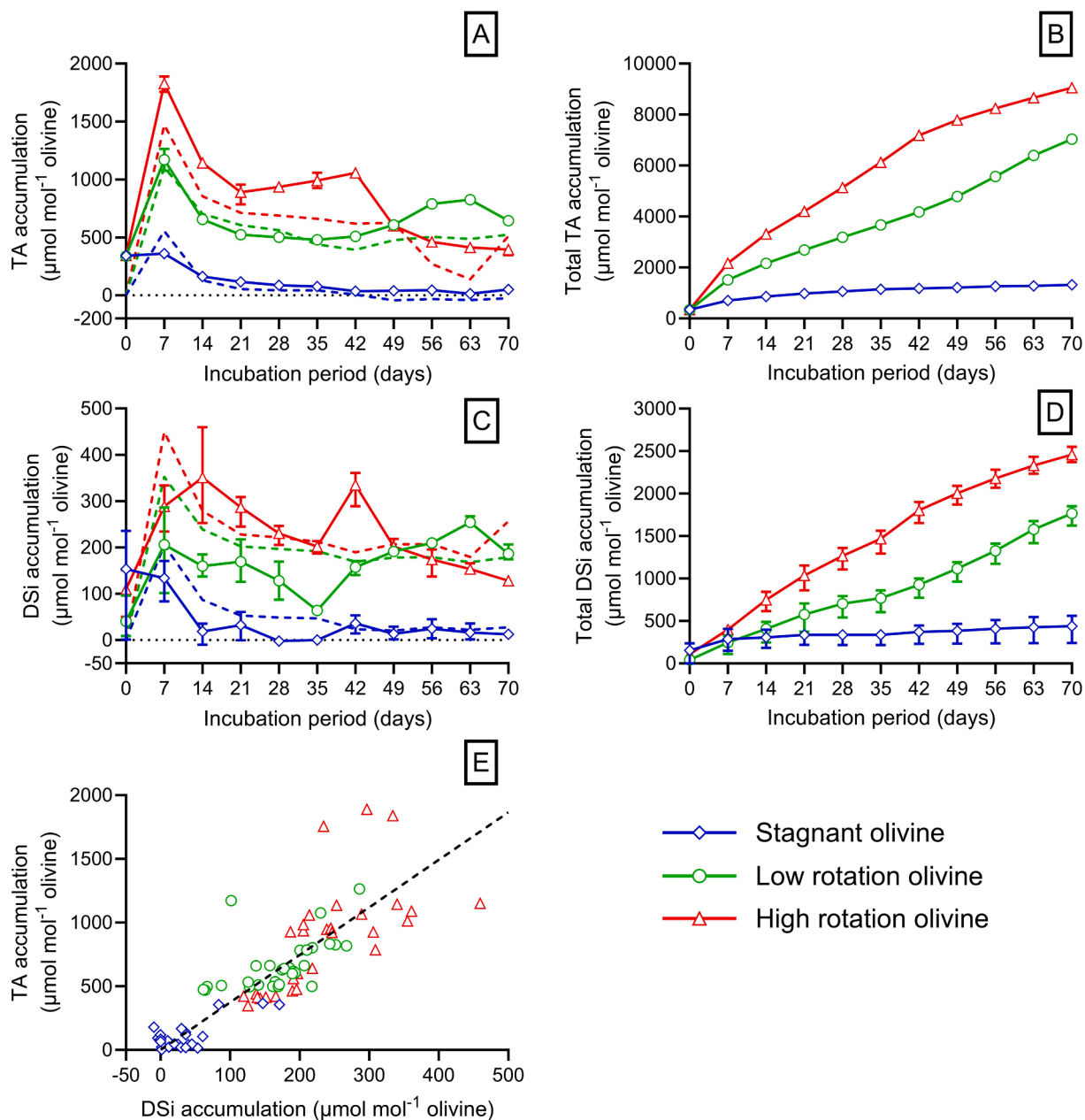


Fig. 2. Weekly (A, C) and cumulative (B, D) accumulation of (A, B) total alkalinity (TA) and (C, D) dissolved (<0.2 μm) seawater. Mean values with range ($N = 3$) are shown. (E) The theoretical (black dashed line, TA/DSi ratio = 3.73) and observed relationship between TA accumulation (μmol) and DSi accumulation (μmol) is given. (A, C) Dashed lines for TA and DSi accumulation represent kinetic box model results.

0.29–0.42 or $\Omega(t_k) = 1.9$ –2.6). Immediately after the start, the stagnant olivine treatment showed a marked increase in aragonite $SI(t_k)$ ($SI(t_k) \approx 0.58$ or $\Omega(t_k) \approx 3.8$) compared to the seawater control (Fig. 3B), after which it gradually decreased to the seawater control values (Fig. 3B). In the low rotation and high rotation treatments, the aragonite $SI(t_k)$ also showed a steep initial increase, but remained elevated and varied between 0.49 and 0.90 ($\Omega(t_k) = 3.1$ –8.0) (Fig. 3B).

The $SI(t_k)$ for forsterite (Mg_2SiO_4) remained relatively constant and was negative throughout the experiment, thus indicating conditions that promote olivine dissolution (Fig. 3D). Between day 14 and 35, DSi concentrations dropped below the detection limit (0.36 $\mu\text{mol/L}$) thus providing anomalous $SI(t_k)$ values in the controls. The $SI(t_k)$ for amorphous ferrihydrite was negative for the seawater control and close to 0 for the olivine treatments throughout the experiment (Fig. 3C). However, these $SI(t_k)$ values should be interpreted with caution since high dissolved Fe concentration in olivine treatments (Supplementary

Fig. S3D) suggest sampling of nanoparticulate $\text{Fe}(\text{OH})_3$. The $SI(t_k)$ for sepiolite was relatively constant in the rotation treatments and remained at an elevated values ($SI(t_k) = 1.5$ –7.8 or $\Omega(t_k) = 32$ –6.3E+07) throughout the experiment (Fig. 3E), thus signifying the potential of sepiolite formation. The $SI(t_k)$ values of talc ($\text{Mg}_3\text{Si}_4\text{O}_{10}(\text{OH})_2$), chrysotile ($\text{Mg}_3\text{Si}_2\text{O}_5(\text{OH})_4$), calcite (CaCO_3) and amorphous silica ($\text{SiO}_2(\text{am})$) are shown in Supplementary Fig. S2.

3.3. Grain scale dissolution features

The olivine surface Mg/Si ratio was analysed to assess the presence of cation depleted layers which could significantly reduce mineral reactivity (Meysman and Montserrat, 2017; Oelkers et al., 2018). The Mg/Si ratio on individual olivine grains showed considerable variation, ranging between 1.0 and 3.1 in all olivine treatments (Fig. 4A). The median Mg/Si ratio was significantly higher in the stagnant (2.26, $P <$

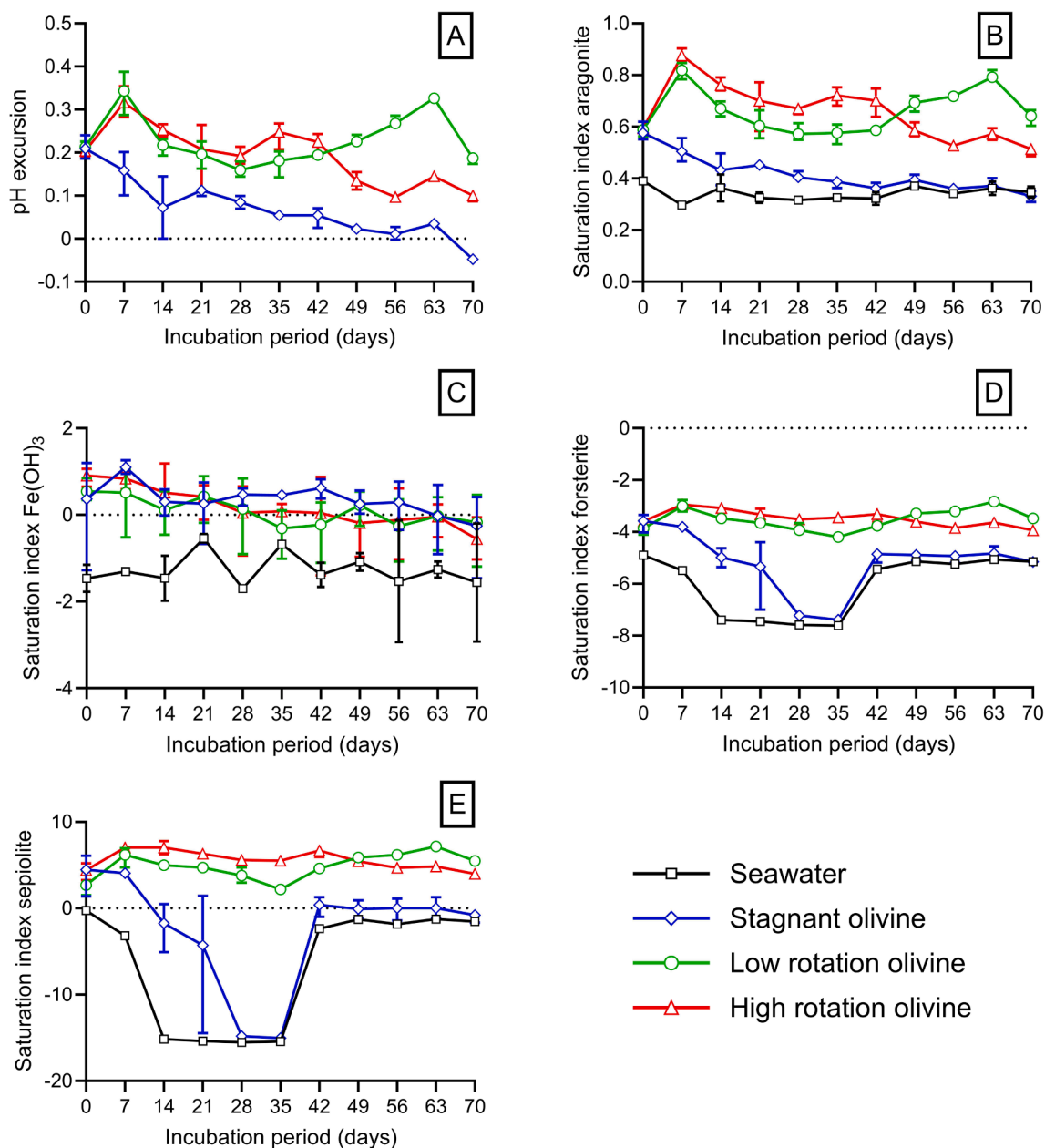


Fig. 3. Weekly excursion of (A) seawater pH, and temporal evolution of (B) aragonite, (C) Fe(OH)₃, (D) forsterite (Mg₂SiO₄), and (E) sepiolite saturation indices calculated from experimental data in PHREEQC V3 using the LNLL database. Mean values with range for olivine treatments (N = 3) and seawater control (N = 2) are shown.

0.001), and high rotation (2.25, $P = 0.0071$) treatment, but not the low rotation treatment (2.16, $P = 0.23$) compared to fresh olivine (2.12) (Fig. 4A). It is important to note that differences in median Mg/Si ratios were relatively small, even though they were found to be statistically significant. Fresh olivine grains analysed via SEM-EDX showed smooth/featureless grain surfaces, angular edges, and a large variation in grain shapes (ranging from rod-like to spherical) (Supplementary Fig. S8A–C). The fresh olivine also showed a small amount of alteration products (possibly hydrous minerals like serpentine, chlorite, or amphibole), which likely developed during natural long-term weathering before the dunite was mined (Supplementary Fig. S9) (Jung et al., 2020; Jung et al., 2021). Some of the fresh olivine grains exhibited cracks and damaged grain edges, which may originate from the mechanical crushing process during dunite sand production (Supplementary Fig. S9). Olivine grains that were retrieved from the rotation treatments at the end of the experiment showed an increase in surface dissolution features (e.g. etch

pits and striation-like features) compared to fresh and stagnant olivine (Fig. 4C–E and Supplementary Figs. S8 and S9). Additionally, damaged grain edges and a higher abundance of microcracks were observed inside some of the weathered olivine grains compared to fresh olivine grains (Fig. 4B and Supplementary Fig. S9). Still, we could not establish a significant statistical difference in microcrack frequency or size between stagnant and rotation treatments (Supplementary Fig. S9).

SEM images of fresh olivine grains revealed the presence of small ($\leq 10 \mu\text{m}$) adhering olivine particles on larger grains (Figs. 4C and 5A). These small particles were absent on olivine recovered from stagnant and rotation treatments at the end of the experiment (Figs. 4D–E and 5A). The median (D_{50}) and 90th percentile (D_{90}) grain diameter (D_{50}) decreased significantly in the stagnant ($D_{50} = 133 \mu\text{m}$, $P = 0.049$, $D_{90} = 210 \mu\text{m}$, $P = 0.010$) and low rotation ($D_{50} = 134 \mu\text{m}$, $P = 0.024$, $D_{90} = 210 \mu\text{m}$, $P = 0.0070$) treatments compared to fresh olivine ($D_{50} = 136 \mu\text{m}$, $D_{90} = 216 \mu\text{m}$). For the 10th percentile grain diameter (D_{10}),

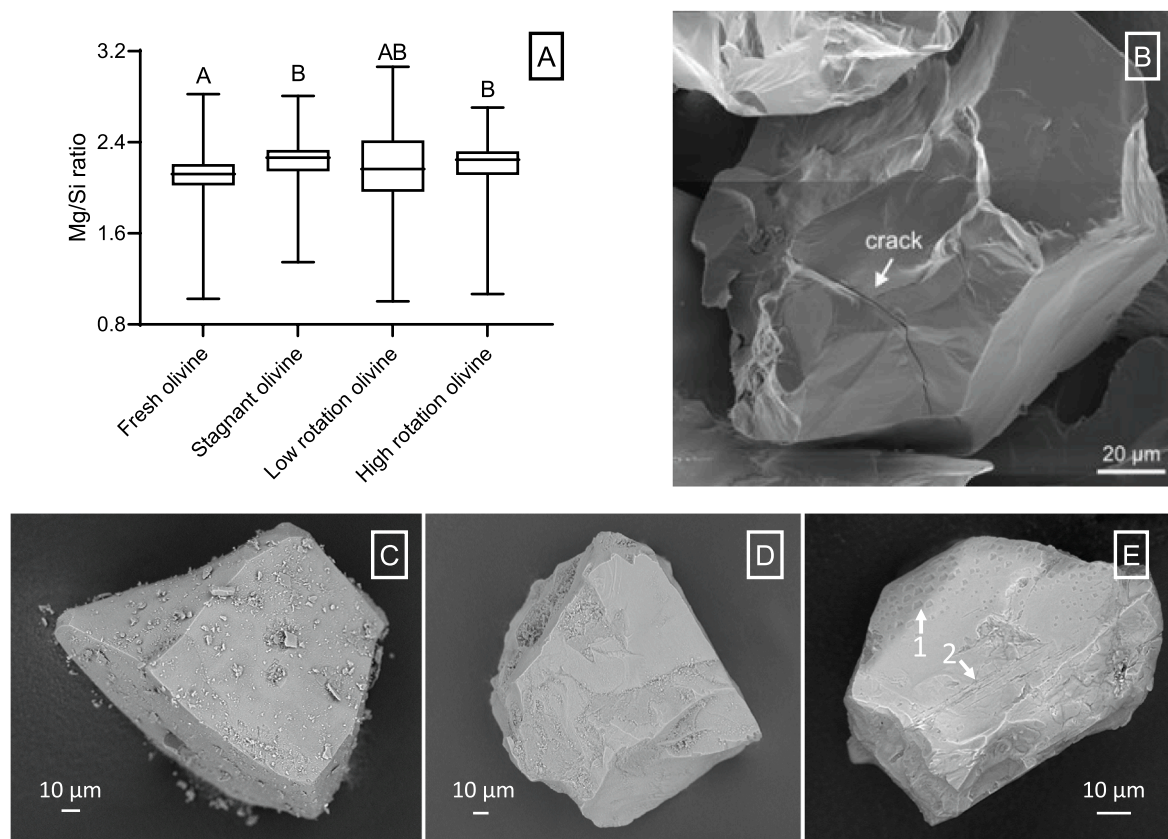


Fig. 4. (A) Box and whisker plots of the magnesium to silicon (Mg/Si) ratio on the surface of fresh ($N = 100$ spots) and experimental olivine grains ($N = 50$ spots), and scanning electron microscopy (SEM) images of (B) a cracked olivine grain of the high rotation treatment, olivine grain of the (C) fresh, (D) stagnant, and (E) high rotation treatment. Note the presence of small adhering particles on fresh olivine (C) and etch pits (E-1) and striation-like features (E-2) on weathered olivine. Whiskers in (A) represent the minimum and maximum Mg/Si ratio.

no significant differences among treatments were found ($H(3) = 3.74$, $P = 0.29$). No significant difference in $D10$, $D50$, or $D90$ was observed among recovered experimental olivine samples (Fig. 5A).

Over time, a shift towards larger suspended sediment particles was observed in the high rotation treatment (Fig. 5B). SEM-EDX analysis showed that suspended particles were mainly olivine (Fig. 5C). Secondary minerals were not found, although they were possibly present in minor amounts given the supersaturated conditions (Fig. 3). At day 0, water samples taken after stirring and subsequent settling for 20 s were dominated by olivine particles smaller than $16 \mu\text{m}$ (Fig. 5B, C). The median suspended grain diameter increased from $10 \mu\text{m}$ at day 0 to $51 \mu\text{m}$ at day 70 (Fig. 5B). Similar trends were observed for the stagnant and low rotation treatments and are discussed in supplementary section SI 2.6. Loss of suspended particles during weekly sampling and water renewals likely explains the shift towards larger suspended grains. According to Stokes' law, all grains with a diameter smaller than $70 \mu\text{m}$ (6% of the total sediment volume) could have been removed during sampling (supplementary section SI 2.6). However, observed total loss of dunite mass was more limited ($2.1 \pm 0.44 \text{ wt\%}$, Table S3).

3.4. Trace metal release

A relatively constant weekly Ni accumulation was observed in the stagnant treatment ($\Delta \hat{N}_{\text{DNI}}^k = 1.2 \mu\text{mol mol}^{-1}$ olivine; range 0.59 – $1.7 \mu\text{mol mol}^{-1}$ olivine) (Fig. 6A). Until day 28, dissolved Ni accumulations did not differ significantly among olivine treatments (Fig. 6A). Afterwards Ni accumulations were significantly higher in the rotation treatments compared to the stagnant treatment, following a similar temporal

trend as dissolved Si accumulations (Fig. 2C).

Dissolved chromium (DCr) accumulation was approximately 10 times lower than DNI accumulation (Fig. 6B). It was elevated, but variable at the start of the experiment, and then decreased, with no significant difference among olivine treatments ($\Delta \hat{N}_{\text{DCr}}^k = -0.017 - 0.31 \mu\text{mol mol}^{-1}$ olivine) (Fig. 6B). From day 49 onwards, DCr concentrations remained below detection limit (0.38 nmol/L) in all treatments (Fig. 6B). Results for other metals (Fe, Cu, Cd, Zn, Pb, and Mn) and major elements (Na, Mg, Ca, and K) can be found in supplementary information (Sections SI 2.2 and SI 2.3).

3.5. CO_2 sequestration

Our results showed that CO_2 was sequestered from the atmosphere in response to an increased TA accumulation. DIC accumulation in the stagnant treatment remained low throughout the experiment (Fig. 7A). The limited DIC accumulation during the first days of the experiment can be explained by the relatively slow CO_2 invasion in seawater given the reduced $p\text{CO}_2$ values in all olivine treatments compared to the seawater control (Fig. 7C) (Kuss and Schneider, 2004; Sarmiento, 2013). DIC accumulations were significantly higher in the rotation treatments and peaked at day 7. The mean DIC accumulation was $457 \mu\text{mol mol}^{-1}$ olivine ($\Delta \hat{N}_{\text{DIC}}^k = 58$ – $791 \mu\text{mol mol}^{-1}$ olivine) in the low rotation and $624 \mu\text{mol mol}^{-1}$ olivine ($\Delta \hat{N}_{\text{DIC}}^k = 67$ – $1297 \mu\text{mol mol}^{-1}$ olivine) in the high rotation treatment (Fig. 7A). Similar to the DSI and TA results, mean DIC accumulation was significantly higher in the high rotation compared to the low rotation treatment until day 42 (Fig. 7A).

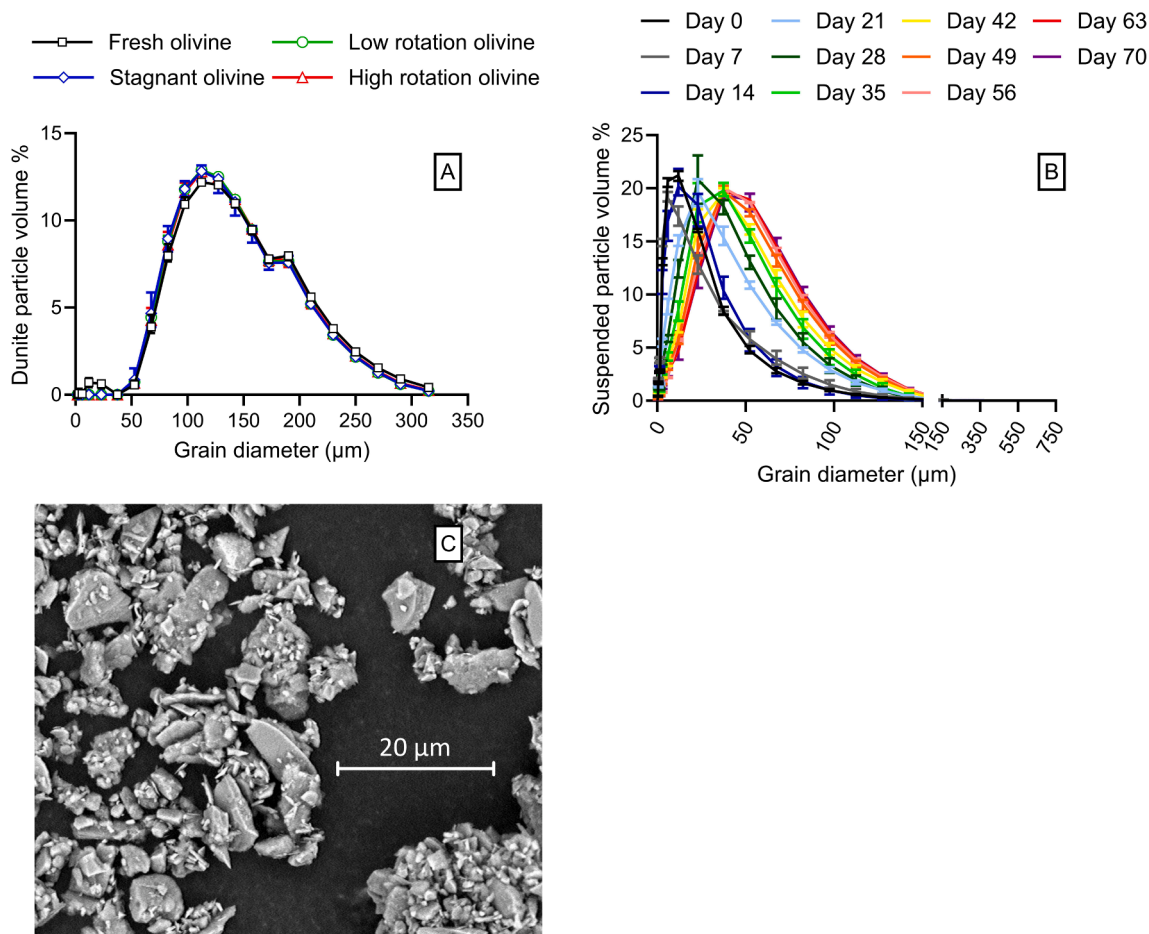


Fig. 5. (A) Volumetric dunite grain size distribution of fresh (N = 5) and weathered (N = 6) dunite grains (mean and range). (B) Volumetric grain size distribution of suspended sediment for the high rotation treatment at different time points (Mean and range, N = 1–3). (C) scanning electron microscopy (SEM) image of representative grains from the suspended sediment in the high rotation treatment at day 7.

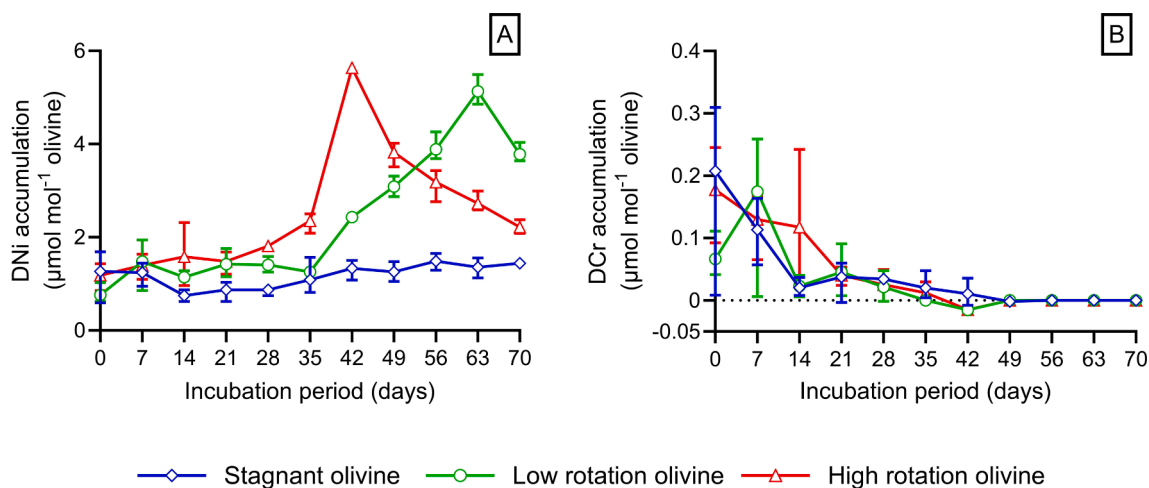


Fig. 6. (A) Weekly evolution of dissolved (<0.2 μm) nickel (DNI) and (B) chromium (DCr) accumulation in natural filtered (<0.2 μm) seawater. Mean values with range (N = 3) are shown.

TA increases clearly resulted in DIC increases in the rotation treatments (Fig. 7B). Theoretical CO₂ sequestration efficiency (γ_{CO_2}) at the experimental conditions, assuming a constant seawater CO₂ fugacity (f_{CO_2}) of 420 μatm, was on average 0.82 mol CO₂ mol⁻¹ TA (dashed line in Fig. 7B). This theoretical CO₂ sequestration efficiency matches the DIC to TA ratio as seen in the data (Fig. 7B), suggesting that the seawater solutions equilibrated with the atmosphere ($p_{CO_2} \approx 420 \mu\text{atm}$) during

the rotation experiments. Equilibration of the seawater carbonate system with the atmosphere was confirmed by p_{CO_2} values that were only slightly lower in the olivine treatments (243–514 μatm, N = 99) compared to the seawater control (418–533 μatm, N = 22) on most sampling days (Fig. 7C). Notably, the lowest p_{CO_2} values were observed in the low rotation treatment (Fig. 7C).

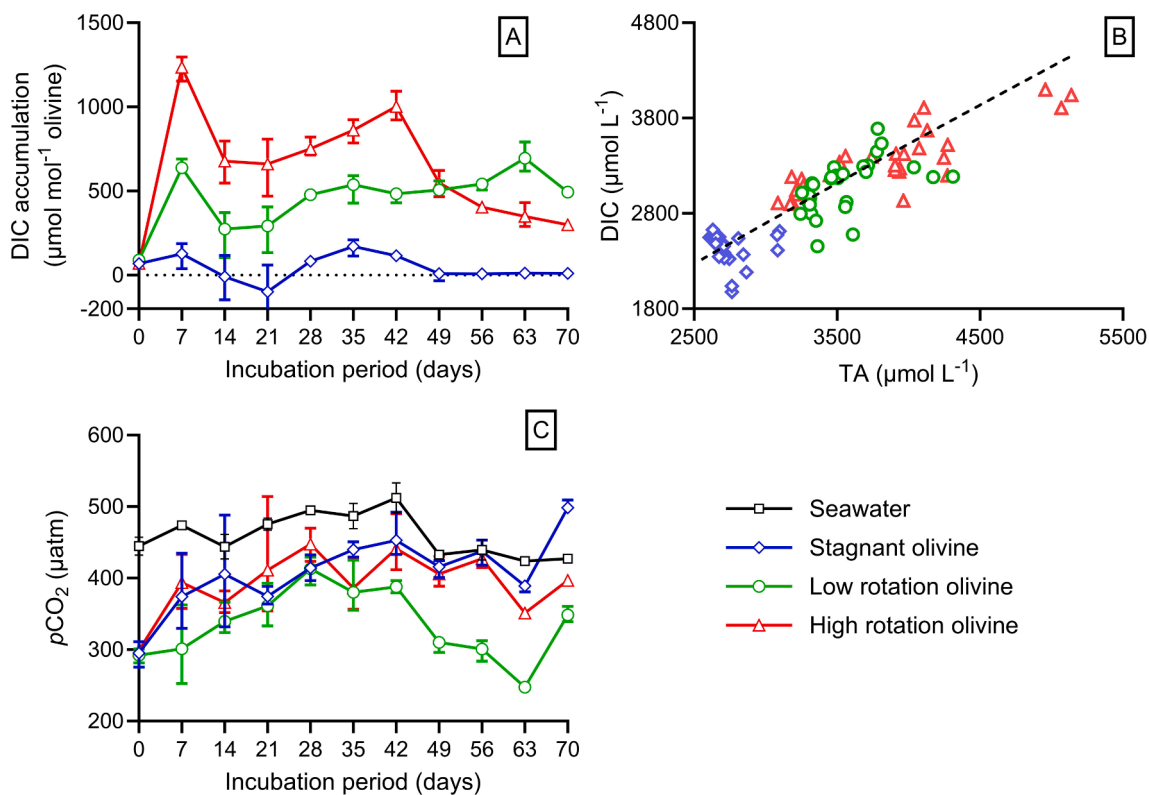


Fig. 7. Weekly evolution of (A) dissolved ($<0.2 \mu\text{m}$) inorganic carbon (DIC) accumulation and (C) partial pressure of CO_2 ($p\text{CO}_2$) in natural filtered ($<0.2 \mu\text{m}$) seawater. Mean values with range for olivine treatments ($N = 3$) and seawater control ($N = 2$) are shown. (B) Theoretical (at $f\text{CO}_2 = 420 \mu\text{atm}$, black dashed line) and observed relationship between dissolved inorganic carbon (DIC) and total alkalinity (TA) concentrations.

3.6. Olivine dissolution rate constants

Dissolution rate constants k_i were derived for different olivine reaction products from observed weekly accumulations (as shown in Fig. 8 and Supplementary Fig. S5). Olivine k_i values for DSi, TA and DIC were

relatively similar within treatments suggesting stoichiometric olivine dissolution (Fig. 8A). Olivine k_i values derived from DNi accumulations were considerably higher and showed more temporal variation than those derived from TA, DIC and DSi, as was previously observed in the study by [Montserrat et al. \(2017\)](#) (Fig. 8A).

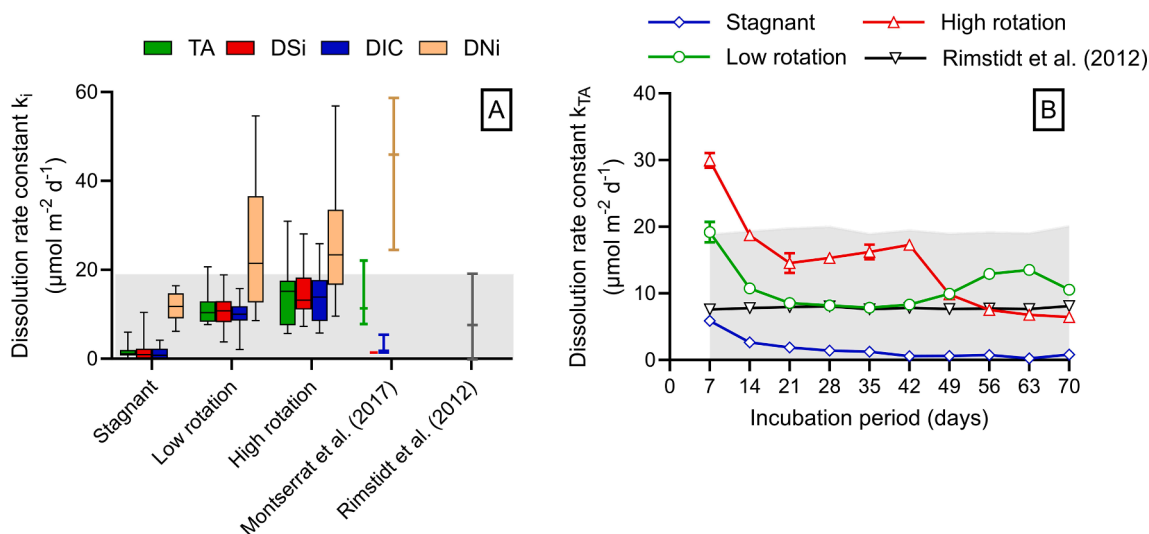


Fig. 8. (A) Box and whisker plots of the olivine dissolution rate constants k_i ($\mu\text{mol m}^{-2} \text{d}^{-1}$) in natural filtered ($<0.2 \mu\text{m}$) seawater ($N = 30$) during the 70-day experiment (whiskers indicate the range). Values were derived from weekly accumulation of total alkalinity (TA, in green), dissolved silicon (DSi, in red), dissolved inorganic carbon (DIC, in blue), and dissolved nickel (DNi, in orange) normalized for reaction stoichiometry (supplementary section SI 1.2). For comparison, olivine k_i values derived by [Montserrat et al. \(2017\)](#) (median and range, $N = 4$) and [Rimstidt et al. \(2012\)](#) (predicted values and propagated errors represented as a line and shading in grey) are shown. Values reported by [Montserrat et al. \(2017\)](#) were temperature normalized (to 15°C) using the Arrhenius equation and activation energy (79.5 kJ mol^{-1}) provided by [Wogelius and Walther \(1992\)](#). (B) weekly evolution of olivine k_{TA} values in natural filtered ($<0.2 \mu\text{m}$) seawater. Mean and range values are shown ($N = 3$). Expected weekly olivine k_i values by [Rimstidt et al. \(2012\)](#) and propagated errors are shown in grey (line and shading).

Based on TA, DSI and DIC accumulations, median k_i values in the stagnant treatment ($0.80\text{--}1.1 \mu\text{mol m}^{-2} \text{d}^{-1}$) were $\sim 8\text{--}14$ times lower compared to the low rotation treatment ($9.1\text{--}10.8 \mu\text{mol m}^{-2} \text{d}^{-1}$), and $\sim 12\text{--}19$ times lower compared to the high rotation treatment ($13.2\text{--}15.2 \mu\text{mol m}^{-2} \text{d}^{-1}$). Therefore, continuous rotation increased olivine k_i values by a factor of $8\text{--}19$ (Fig. 8A). For the high rotation treatment, median k_i values were up to 1.7 times higher compared to the low rotation treatment (Fig. 8A). In comparison to the average predicted k_i values by Rimstidt et al. (2012), observed median k_i values were 7–10 times lower in the stagnant treatment and 1.3–2.8 times higher in the rotation treatments (Fig. 8A). Nevertheless, the range of observed k_i values overlap considerably with predictions by Rimstidt et al. (2012), indicating good agreement between values (Fig. 8A).

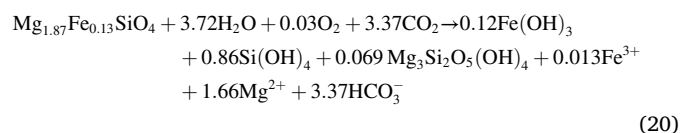
Temporal changes in k_{TA} are displayed in Fig. 8B, while k_{Si} , k_{DIC} and k_{Ni} values are discussed in detail in supplementary section SI 2.4. In general, highest values for k_{TA} are observed in the first two accumulation sessions (Fig. 8B), after which the value in the rotation treatments remains relatively constant (apart from the conspicuous baseline shift at day 42). The k_{TA} in the stagnant treatment gradually decreases over the successive accumulation sessions. A similar temporal trend was observed for k_{Si} and k_{DIC} (Supplementary Fig. S5).

3.7. Kinetic model simulations

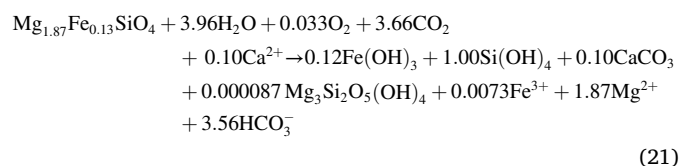
Modelled TA and DSI accumulations reflect observed values reasonably well, although temporal fluctuations in the rotation treatments could not be accurately simulated (dashed lines in Fig. 2A and C). The model underestimated TA production in the high rotation treatment (Fig. 2A) and overestimates DSI accumulation in the low rotation treatment (Fig. 2C). At the end of the experiment the model predicted a total amount of dissolved olivine of 0.69, 2.32, and 2.84 mmol in the stagnant, low rotation, and high rotation treatments, respectively (indicating that 0.07%, 0.25%, and 0.31% of the initially present olivine was dissolved). The rate controlling pre-factor k_{rc} (supplementary Eq. (11)) implemented in the rate equation by Rimstidt et al. (2012) that gave the best model fit to the data was 0.43 in the stagnant, 2.0 in the low rotation, and 2.3 in the high rotation treatment.

Our model simulations suggest limited secondary mineral precipitation. For all olivine treatments, 0.12 mol $\text{Fe}(\text{OH})_3$ precipitation occurred per mol of dissolved olivine (Eqs. (20–22)). In the low rotation treatment, formation of 0.086 mol chrysotile mol^{-1} olivine and 0.10 mol aragonite mol^{-1} olivine were simulated (Eq. (21)). For the high rotation treatment this was 0.015 mol chrysotile mol^{-1} olivine and 0.22 mol aragonite mol^{-1} olivine (Eq. (22)). In the stagnant treatment 0.069 mol mol^{-1} olivine chrysotile formation was modelled (Eq. (20)). Overall, modelled secondary mineral precipitation resulted in an 11–19% decrease of the TA production by olivine dissolution. The reaction stoichiometry derived from modelled olivine dissolution and secondary mineral precipitation is as follows:

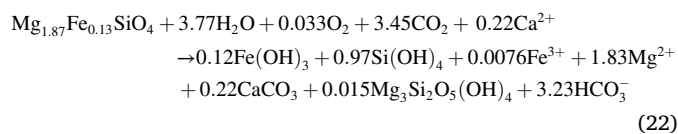
Stagnant olivine:



Low rotation olivine:



High rotation olivine:



4. Discussion

4.1. Collision enhances olivine dissolution in seawater

We investigated the effect of continuous grain tumbling on olivine dissolution kinetics in seawater and hypothesized that increasing physical stress would enhance olivine dissolution through increased particle fragmentation. Significantly higher TA and DSI accumulation in the rotation treatments compared to the stagnant treatment (Fig. 2A–D) confirm that continuous grain tumbling enhanced olivine dissolution. Derived olivine dissolution rate constants showed that continuously tumbled olivine dissolved approximately 8 to 19 times faster than stagnant olivine (Fig. 8). Four processes can potentially explain this enhanced weathering in our study, namely (I) grain fragmentation induced by abrasion, (II) removal of passivating layers upon grain-grain collisions, (III) rate limiting air-seawater CO_2 exchange under stagnant conditions, and (IV) flushing of reaction products from the pore solution by sediment movement.

Grain fragmentation enhances olivine dissolution by increasing the effective surface area (Oelkers et al., 2018; Rigopoulos et al., 2018). However, no significant change in olivine grain size distribution was observed (Fig. 5A), indicating that grain fragmentation was limited in our 70-day study. Previous studies have observed extensive olivine cracking and fragmentation at high temperature ($200 \text{ }^\circ\text{C}$) or low pH (pH = 1.5) solutions (Varadachari et al., 1994; Lafay et al., 2018). However, in our experiment, olivine dissolution took place at seawater pH ≈ 8.2 and ambient temperature of $\approx 15 \text{ }^\circ\text{C}$. Under these mild conditions, it is expected that internal micro cracks and grain fragmentation will only develop over time scales of years (Hangx and Spiers, 2009).

Continuous grain tumbling can also prevent formation of passivating layers on olivine grains, such as amorphous silica ($\text{SiO}_2(\text{am})$) or iron hydroxides ($\text{Fe}(\text{OH})_3$). These passivating layers slow down dissolution by decreasing the olivine-fluid interfacial area and increasing the diffusion distance towards the active dissolution zone (Béarat et al., 2006; Daval et al., 2011; Schuiling and De Boer, 2011; Maher et al., 2016; Griffioen, 2017; Meysman and Montserrat, 2017). Under-saturation of the bulk solution with regards to $\text{SiO}_2(\text{am})$ (Supplementary Fig. S2D) indicates that passivating $\text{SiO}_2(\text{am})$ layer formation was implausible. However, the pore water of the stagnant treatment could have been supersaturated with respect to $\text{SiO}_2(\text{am})$, resulting in thin passivating layer formation that could be undetectable with SEM. Nevertheless, removal of brittle $\text{SiO}_2(\text{am})$ layers during weekly water renewals likely prevented significant passivation of olivine surfaces (Béarat et al., 2006). A similar fate is expected for any $\text{Fe}(\text{OH})_3$ crystals that inevitably formed given that they were not observed via SEM-EDX analysis. Preferential Mg release at pH ≤ 8.8 can lead to the rapid formation of cation depleted layers on olivine grains (Seyama et al., 1996; Pokrovsky and Schott, 2000b, 2000a; Montserrat et al., 2017). In our experiment, the olivine surface Mg/Si ratios differed only slightly between treatments (Fig. 4A), indicating that extensive cation depleted layers were not formed. Nevertheless, a relatively large variation in Mg/Si ratio was observed on individual olivine grains, confirming spatial variability in composition and surface reactivity (Rimstidt et al., 2012; Oelkers et al., 2018). Overall, we assert that removal of passivating layers was not the prime enhancement factor of olivine dissolution in our experiment.

Waves and currents are essential for ocean mixing (Moum, 2021), which is a pivotal process for CESW since it drives transport of alkalinity enriched bottom water to the surface ocean for CO_2 uptake and

equilibration (Bach et al., 2023). This CO₂ equilibration prevents high seawater pH excursions that could be harmful for marine biota and slow down olivine dissolution (Bach et al., 2019). Here, seawater pCO₂ values were lowest in the low rotation treatment (Fig. 7C) likely as a result of slower water movement compared to the high rotation treatment. Importantly, seawater pCO₂ values in the stagnant treatment were generally close to atmospheric pCO₂ (~420 μatm) and not significantly lower compared to the rotation treatments (Fig. 7C), indicating that low olivine dissolution rates were not the result of slow CO₂ equilibration.

Finally, olivine dissolution can be impeded by saturation of the surrounding water, and so flushing of reaction products from the olivine-seawater interface could enhance dissolution (Meysman and Montserrat, 2017; Montserrat et al., 2017). Previous studies have shown that advective pore water flow can enhance solute fluxes to the overlying water by up to 50-fold compared to stagnant conditions (Precht and Huettel, 2003; Cook et al., 2007; Santos et al., 2012). Under stagnant conditions, molecular diffusion towards the grain interface can be rate controlling. We did not directly assess the concentration of reaction product accumulation and saturation indices in the pore water of the stagnant treatment. However, given limited particle fragmentation, implausible passivating layer formation, and no rate limiting seawater CO₂ influx, enhanced weathering in our rotation treatments appears to be mainly driven by pore water flushing. This conclusion is supported by previous studies which showed that silicate weathering rates are directly proportional to solute transport rates for systems with a water residence time longer than two days (Maher, 2010; Yu and Hunt, 2017).

4.2. Temporal variation in olivine dissolution rates

The rate of olivine dissolution was not constant with time in our 70-day experiment (Fig. 8B). An immediate increase in seawater pH, TA and DSi accumulation was observed in all olivine treatments after adding the olivine to the seawater solution (Figs. 2A, D, and 3A). This “dissolution spike” can be explained by the rapid (within minutes) exchange of Mg²⁺ or other divalent cations (e.g. Ni²⁺, Fe²⁺) for protons (H⁺) in the first one or two monolayers of the olivine grain surfaces (Luce et al., 1972; Blum and Lasaga, 1988; Oelkers et al., 2018). However, in our experiment the “dissolution spike” was sustained over a much longer period (first two weeks). We also noticed that fresh olivine grains were covered with fine adhering particles (≤10 μm), which likely are formed during crushing of olivine rich rocks for sand production (Fig. 4C). Weathering of these fines likely explains the prolonged DSi accumulation and high TA, pH, and DIC accumulation within the first two weeks of the experiment (Figs. 2A, D, 3A, and 7A).

A decreased olivine reactivity was observed from day 42 and 63 onwards in the high rotation and low rotation treatments, respectively (Figs. 2A, C and 8B). Given that formation of passivating or cation-depleted layers was highly unlikely for rotated olivine grains, a decrease in surface reactivity could possibly explain the observed results (Grandstaff, 1978; Wogelius and Walther, 1992; Bandstra and Brantley, 2008; Rimstidt et al., 2012). Such a decrease in surface reactivity can be caused by variation in dissolution rates of distinct crystallographic planes (Grandstaff, 1978; Chung-Cherng and Pouyan, 1993; Oelkers et al., 2018). Upon inspection, etch pits were observed on some olivine grains (Fig. 4E and Supplementary Fig. S8K), but not all. Furthermore, striation like features, cracked grain edges and surficial and internal micro-cracks were observed on weathered and fresh olivine grains (Fig. 4B, E and Supplementary Fig. S9).

Our results suggest that stoichiometric olivine dissolution took place in the experiment. Average $\Delta\hat{N}_{TA}^k/\Delta\hat{N}_{DSi}^k$ ratios in the low rotation (4.3 mol TA mol⁻¹ DSi) and high rotation treatment (3.7 mol TA mol⁻¹ DSi) were close to the theoretical value of 3.73 mol TA mol⁻¹ DSi, which accounts for full dissolution of olivine followed by Fe(OH)₃ precipitation (supplementary section SI 1.2). In previous experiments on olivine weathering in seawater, Montserrat et al. (2017) and Fuhr et al. (2022)

observed $\Delta N_{TA}^k/\Delta N_{DSi}^k$ ratios that deviated significantly from the theoretical value. Deviation of the $\Delta N_{TA}^k/\Delta N_{DSi}^k$ ratio from the theoretical value can be explained by (1) incomplete olivine dissolution, (2) dissolution of other minerals in the dunite sand, or (3) precipitation of secondary phases (Fuhr et al., 2022). Therefore, a multiparameter approach, where DSi, TA, DN_i and DIC are conjointly measured, seems advised to monitor olivine dissolution and CO₂ sequestration rates under field conditions (Montserrat et al., 2017).

Experimental olivine dissolution rate constants are within the range of previously reported k_i values (Rimstidt et al., 2012; Montserrat et al., 2017). Yet, estimated k_i values are underestimations due to the loss of the finest olivine particles during weekly water renewals (discussed in supplementary section SI 2.6). At the end of the experiment a loss of olivine mass (by 1.6–2.8 wt%, Supplementary Table S3) and decrease in olivine A_{GEO} (from 0.0161 to 0.0145 m²/g, Supplementary Table S4) was observed which could not be accurately accounted for in weekly k_i value derivation, resulting in an underestimation of derived values by up to 14%.

4.3. Minimal secondary mineral formation

Secondary mineral formation can significantly reduce net alkalinity production and resulting atmospheric CO₂ uptake during olivine weathering (Griffioen, 2017; Meysman and Montserrat, 2017; Montserrat et al., 2017; Oelkers et al., 2018). Previous studies have found contradictory results on the importance of secondary carbonate formation. Rigopoulos et al. (2018) observed only small TIC changes when dunite was weathered in artificial seawater (2 g dunite L⁻¹ for 60 days). Similarly, Montserrat et al. (2017) did not observe a significant TIC increase or aragonite precipitation when olivine was weathered in natural and artificial seawater (8.7–29 g olivine L⁻¹ for up to 137 days). In contrast, Fuhr et al. (2022) observed significant aragonite formation after reacting olivine rich (~75%) sand in artificial seawater (25–100 g ultramafic sand L⁻¹ for 134 days).

Here, we observed no increase in olivine TIC content (Supplementary Fig. S10) or aragonite crystals on weathered olivine grains (Fig. 4 and Supplementary Fig. S8) even though aragonite was supersaturated in the overlying seawater (Fig. 3B). Under natural conditions, seawater is supersaturated with respect to CaCO₃, but precipitation does not occur due to the lack of mineral precipitation nuclei and presence of dissolved organic carbon, Mg²⁺ and phosphate which inhibit precipitation (Morse et al., 2007; Pan et al., 2021; Moras et al., 2022). The threshold SI for aragonite precipitation in seawater is dependent on the availability of precipitation surfaces, being higher in their absence (Moras et al., 2022). In the absence of precipitation surfaces, homogeneous aragonite precipitation would occur at a SI of ~1.26 (Ω ≈ 18) in 25 °C seawater (Sun et al., 2015). In the presence of colloids and organic particles, pseudo-homogenous precipitation of aragonite would be expected at a SI value of ~1.06 (Ω ≈ 11.5) for the experimental seawater (salinity of 33‰ and temperature of 15 °C) (Marion et al., 2009). Furthermore, recently Moras et al. (2022) observed heterogeneous (i.e. on mineral phases) aragonite precipitation on CaO and Ca(OH)₂ particles smaller than 63 μm at a SI value of ~0.85 (Ω ≈ 7) in 21 °C natural seawater (salinity of 35‰). This threshold is very close to SI peak values up to 0.9 observed on day 7 and 63 of our experiment, signifying potential heterogeneous aragonite precipitation. Overall, we can conclude that CaCO₃ precipitation was limited in our study given that aragonite SI values remained below critical thresholds on most sampling days (Fig. 3B).

Secondary precipitation of iron(hydr)oxides inevitably occurred, although Fe(OH)₃ crystals were not observed through SEM analysis, possibly due to removal during weekly water renewals. The experimental olivine contains on average 6.6% fayalite, compared to 93.4% of forsterite (supplementary section SI 1.2). Under oxic conditions, any Fe (II) released during dissolution will be rapidly oxidized to Fe(III) and

precipitated as iron(III) (hydr)oxide (Millero, 1998; Griffioen, 2017; Meysman and Montserrat, 2017; Montserrat et al., 2017). This process hence reduced the total alkalinity production by 6.6% for the olivine employed here (Griffioen, 2017; Montserrat et al., 2017).

Finally, regarding phyllosilicates, seawater was supersaturated with respect to sepiolite, talc, and chrysotile on most sampling days in the olivine treatments (Fig. 3E and Supplementary Fig. S2). However, similar to Montserrat et al. (2017), no phyllosilicate precipitates were observed on olivine grains (Fig. 4B–E and Supplementary Fig. S8) and formation was expected to be low based on the best fitting models for the experimental data (Fig. 2A and C). The combination of weekly water renewals and slow formation kinetics could possibly explain the absence of Mg-silicate precipitates in our experiment (Baldermann et al., 2018).

4.4. Trace metal release

One of the environmental concerns of enhanced olivine weathering in marine conditions is the accumulation of Ni and Cr within the ecosystem (Montserrat et al., 2017; Flipkens et al., 2021). In the crystal structure of olivine, Ni^{2+} substitutes for other divalent cations (e.g. Mg^{2+} and Fe^{2+}) and is present at concentrations ranging from 0.1 to 0.5 wt% (here 0.25 wt%, Table 2) (Thompson et al., 1984; Santos et al., 2015; Lynn et al., 2017). Nickel is an essential trace element for macrophytes and microorganisms, but its essentiality for aquatic animals remains under debate (Muysen et al., 2004; Blewett and Leonard, 2017). Exposure to elevated Ni concentrations can lead to toxicological effects including reduced growth, reproduction and survival as a result of oxidative stress, disruption of ion homeostasis and respiratory impairment (Blewett and Leonard, 2017; Gissi et al., 2020). We observed no significant difference in DNi accumulation among treatments until day 28 (Fig. 6A), which is possibly explained by Ni adsorption to fine suspended olivine particles that were gradually removed during sampling (Kleiv and Thornhill, 2004). Minimal (<1.5%) Ni adsorption to precipitated $\text{Fe}(\text{OH})_3$ particles was expected according to PHREEQC diffuse double layer surface-complexation models assuming $\text{Fe}(\text{OH})_3$ specific surface area ($600 \text{ m}^2/\text{g}$) and binding site availability (0.005 and 0.2 mol/mol for strong and weak sites, respectively) according to Dzombak and More (1990). From day 35 onwards, high non stoichiometric Ni release was observed (Figs. 6A and 8A). In general, our findings are in line with the results of Montserrat et al. (2017), suggesting preferential release of metal cations (Ni^{2+} and Mg^{2+}) compared to Si at seawater pH although this was not evident from Mg/Si ratios on weathered olivine grains (Fig. 4A). Therefore the reason for the high Ni release remains uncertain and requires further research.

Chromium (III) is heterogeneously distributed in olivine containing dunite grains, mainly in the form of chromite (FeCr_2O_4) inclusions (Santos et al., 2015; Bell, 2021), and hence not part of the olivine silicate matrix. Upon olivine dissolution, chromite nanoparticles could be released, which can interact with Mn(IV) oxides resulting in the dissolution of chromite and subsequent oxidation to Cr(VI) or precipitation as Cr(III) hydroxides (Ivarsson et al., 2011; McClenaghan and Schindler, 2022). However, Mn(IV) oxides were likely not present in significant amounts in our experiment since their formation is mainly microbially driven (Tebo et al., 2004). Furthermore, under oxic conditions, Cr(III) released during dissolution could be converted to Cr(VI) as indicated by the high Cr(VI) concentrations found in streams and rivers near chromite and Ni mines (Gunkel-Grillon et al., 2014; Das et al., 2021). While Cr(VI) is considered as a highly mobile human carcinogen, Cr(III) is comparatively less toxic and relatively immobile (Aharchaou et al., 2018). Although the Cr content of the experimental olivine was relatively high (0.30 wt%, Table 2), dissolved Cr accumulation was low in all treatments (Fig. 6B), confirming that most Cr remained in a particulate form.

Overall, our results confirm that Ni is the trace metal of most concern for future CESW applications due to its release as a soluble compound (Montserrat et al., 2017; Flipkens et al., 2021). Low aqueous solubility of

Cr^{3+} infers lower bioavailability compared to Ni (Flipkens et al., 2021), but potential oxidation to Cr^{6+} or accumulation of Cr^{3+} nanoparticles in marine sediment could still pose a risk to marine biota (Gunkel-Grillon et al., 2014; Kanakalakshmi et al., 2017; Das et al., 2021).

4.5. Implications for natural and enhanced marine silicate weathering

The carbonate–silicate geochemical cycle plays a pivotal role in regulating Earth's climate over geological time scales (Penman et al., 2020). Coastal enhanced silicate weathering aims to accelerate this process to help mitigate human-induced climate change (Meysman and Montserrat, 2017). A thorough understanding of factors controlling silicate weathering kinetics under marine conditions is crucial to comprehend the natural carbon cycle and quantify the CDR potential of CESW (Meysman and Montserrat, 2017; Sun et al., 2019). In this regard, our results show that pore water exchange rates can significantly affect silicate mineral dissolution rates in seawater. Hence, hydrodynamic conditions should be considered when quantifying natural silicate weathering rates to obtain a more comprehensive understanding of the Earth's carbon cycle (Maher, 2010; Yu and Hunt, 2017). Additionally, these findings highlight that olivine should ideally be supplied in coastal areas with high bed shear stress and pore water exchange rates to enhance mineral dissolution and CO_2 sequestration.

The present study should be seen as a step towards future experimental olivine weathering studies in flume and mesocosm set-ups that mimic natural conditions more closely. Furthermore, marine olivine toxicity tests are needed to accurately assess environmental impacts of coastal enhanced olivine weathering (Flipkens et al., 2021). If the environmental risk is acceptable larger-scale field trials could be set up to generate field data needed for the more realistic assessment of the CO_2 sequestration potential and scalability of CESW.

5. Conclusions

Coastal enhanced olivine weathering has been put forward as a way to remove atmospheric CO_2 for climate change mitigation. However, the efficiency and environmental impacts of the technique remain to be assessed, since data on olivine dissolution in natural seawater conditions is scarce. Here, we investigated the effect of continuous grain-grain collisions on olivine dissolution and trace metal release kinetics in natural seawater. Olivine dissolution was complete and stoichiometric, while secondary mineral precipitation and passivating layer formation were restricted. Olivine dissolution rate constants were 8 to 19 times higher for rotated olivine compared to stagnant olivine. Seawater CO_2 equilibration was not significantly rate limiting, and grain size distribution analysis suggests that minimal particle fragmentation occurred. Therefore, we infer that advective pore water flushing was the main process enhancing olivine dissolution during this experiment. The presence of micro cracks inside olivine grains suggests that physical agitation could potentially enhance olivine dissolution over longer time scales. Overall, this study shows that coastal hydrodynamics could enhance silicate weathering in a marine environment, which is of importance for both the natural silicon cycle and coastal enhanced olivine weathering. Therefore, olivine should ideally be supplied in dynamic coastal systems with high bed shear stress and pore water exchange rates. However, the question remains how olivine dissolution rates in this laboratory agitation experiment compare to actual rates in coastal ocean settings with complex hydrodynamical conditions and presence of biological processes (e.g. bioturbation and microbial acidification).

Declaration of Competing Interest

The authors declare that they have no known competing financial interests or personal relationships that could have appeared to influence the work reported in this paper.

Acknowledgements

The authors thank Karin Van den Bergh, Saïd De Wolf, and Anne Cools for their help with the DIC, TA and grain size analyses, respectively. Furthermore, we are grateful for the help of Kayawe Valentine Mubiana and Steven Joosen with the metal analyses. Moreover, Karen Leysens, Saskia Defossé, and Vera Meynen are thanked for their help with the analysis and interpretation of the BET surface area results.

Appendix A. Supplementary material

All research data used for construction of the figures is provided in the [supplementary Excel file](#). Dunitite chemical composition, olivine reaction stoichiometry, specific surface area, and mass added to the experimental bottles are provided in the supplementary PDF file. Furthermore, North Sea water chemical composition, salinity, and measured trace element (Zn, Cu, Cd, Fe, and Mn) and major element (Na, Mg, Ca and K) concentrations are shown. To visualize temporal trends in olivine reactivity, the cumulative dissolved olivine and weekly k_i values are given. A detailed description of model calculation and input data are provided together with $SI(t_k)$ values for several secondary phases. Finally, weekly grain size distribution of the suspended olivine and grain scale changes of the weathered olivine are illustrated. Supplementary material to this article can be found online at <https://doi.org/10.1016/j.gca.2023.09.002>.

References

Aharchaoui, I., Py, J.S., Cambier, S., Loizeau, J.L., Cornelis, G., Rousselle, P., Battaglia, E., Vignati, D.A., 2018. Chromium hazard and risk assessment: New insights from a detailed speciation study in a standard test medium. *Environ. Toxicol. Chem.* 37 (4), 983–992.

Albright, R., Caldeira, L., Hosfelt, J., Kwiatkowski, L., Maclaren, J.K., Mason, B.M., Nebuchina, Y., Ninokawa, A., Pongratz, J., Ricke, K.L., 2016. Reversal of ocean acidification enhances net coral reef calcification. *Nature* 531 (7594), 362–365.

Bach, L.T., Gill, S.J., Rickaby, R.E., Gore, S., Renforth, P., 2019. CO₂ removal with enhanced weathering and ocean alkalinity enhancement: Potential risks and co-benefits for marine pelagic ecosystems. *Front. Clim.* 1, 7.

Bach, L.T., Ho, D.T., Boyd, P.W., Tyka, M.D., 2023. Toward a consensus framework to evaluate air–sea CO₂ equilibration for marine CO₂ removal. *Limnol. Oceanogr. Lett.*

Baldermann, A., Mavromatis, V., Frick, P.M., Dietzel, M., 2018. Effect of aqueous Si/Mg ratio and pH on the nucleation and growth of sepiolite at 25 °C. *Geochim. Cosmochim. Acta* 227, 211–226.

Bandstra, J.Z., Brantley, S.L., 2008. Surface evolution of dissolving minerals investigated with a kinetic Ising model. *Geochim. Cosmochim. Acta* 72 (11), 2587–2600.

Bates, N.R., Samuels, L., Merlivat, L., 2001. Biogeochemical and physical factors influencing seawater fCO₂ and air–sea CO₂ exchange on the Bermuda coral reef. *Limnol. Oceanogr.* 46 (4), 833–846.

Béarat, H., McKelvy, M.J., Chizmeshya, A.V., Gormley, D., Nunez, R., Carpenter, R., Squires, K., Wolf, G.H., 2006. Carbon sequestration via aqueous olivine mineral carbonation: role of passivating layer formation. *Environ. Sci. Tech.* 40 (15), 4802–4808.

Bell, A.S., 2021. Chromium redox systematics in basaltic liquids and olivine. In: Moretti, R., Neuville, D.R. (Eds.), *Magma Redox Geochemistry*, pp. 165–176.

Blewett, T.A., Leonard, E.M., 2017. Mechanisms of nickel toxicity to fish and invertebrates in marine and estuarine waters. *Environ. Pollut.* 223, 311–322.

Blum, A., Lasaga, A., 1988. Role of surface speciation in the low-temperature dissolution of minerals. *Nature* 331 (6155), 431–433.

Chung-Cheng, L., Pouyan, S., 1993. Directional dissolution kinetics of willemite. *Geochim. Cosmochim. Acta* 57 (1), 27–35.

Cook, P.L., Wenzhöfer, F., Glud, R.N., Janssen, F., Huettel, M., 2007. Benthic solute exchange and carbon mineralization in two shallow subtidal sandy sediments: Effect of advective pore-water exchange. *Limnol. Oceanogr.* 52 (5), 1943–1963.

Cripps, G., Widdicombe, S., Spicer, J.L., Findlay, H.S., 2013. Biological impacts of enhanced alkalinity in *Carcinus maenas*. *Mar. Pollut. Bull.* 71 (1–2), 190–198.

Das, P.K., Das, B.P., Dash, P., 2021. Chromite mining pollution, environmental impact, toxicity and phytoremediation: A review. *Environ. Chem. Lett.* 19 (2), 1369–1381.

Daval, D., Sissmann, O., Menguy, N., Saldi, G.D., Guyot, F., Martinez, I., Corvisier, J., Garcia, B., Machouk, I., Knauss, K.G., 2011. Influence of amorphous silica layer formation on the dissolution rate of olivine at 90 °C and elevated pCO₂. *Chem. Geol.* 284 (1–2), 193–209.

Dickson, A.G., Sabine, C.L., Christian, J.R., 2007. Guide to best practices for ocean CO₂ measurements, North Pacific Marine Science Organization, Sidney, British Columbia. 191pp. (PICES Special Publication 193; IOCCP Report 198).

Dzombak, D.A., More, F.M.M., 1990. Surface Complexation Modelling: Hydrous Ferric Oxide. John Wiley & Sons, New York, p. 416.

Ferderer, A., Chase, Z., Kennedy, F., Schulz, K.G., Bach, L.T., 2022. Assessing the influence of ocean alkalinity enhancement on a coastal phytoplankton community. *Biogeosci. Disc.* 1–36.

Flipkens, G., Blust, R., Town, R.M., 2021. Deriving nickel (Ni (II)) and chromium (Cr (III)) based environmentally safe olivine guidelines for coastal enhanced silicate weathering. *Environ. Sci. Tech.* 55 (18), 12362–12371.

Next, we would like to thank Miguel Portillo Estrada for his assistance with the TIC analysis and Arthur Vienne for his instructions on PHREEQC calculations. Finally, we thank the anonymous reviewers for their constructive comments that improved the quality of this manuscript. This study was financially supported by the Fonds voor Wetenschappelijk Onderzoek-Vlaanderen (FWO) SBO Project S000619N (Negative Emissions through Enhanced Mineral Weathering in the Coastal Zone).

Fuhr, M., Geilert, S., Schmidt, M., Liebetrau, V., Vogt, C., Ledwig, B., Wallmann, K., 2022. Kinetics of olivine weathering in seawater: an experimental study. *Front. Clim.* 39.

Gim, B.M., Hong, S., Lee, J.S., Kim, N.H., Kwon, E.M., Gil, J.W., Lim, H.H., Jeon, E.C., Khim, J.S., 2018. Potential ecotoxicological effects of elevated bicarbonate ion concentrations on marine organisms. *Environ. Pollut.* 241, 194–199.

Gissi, F., Wang, Z., Batley, G.E., Leung, K.M., Schlegel, C.E., Garman, E.R., Stauber, J.L., 2020. Deriving a chronic guideline value for nickel in tropical and temperate marine waters. *Environ. Toxicol. Chem.* 39 (12), 2540–2551.

Gore, S., Renforth, P., Perkins, R., 2019. The potential environmental response to increasing ocean alkalinity for negative emissions. *Mitig. Adapt. Strateg. Glob. Chang.* 24 (7), 1191–1211.

Grandstaff, D., 1978. Changes in surface area and morphology and the mechanism of forsterite dissolution. *Geochim. Cosmochim. Acta* 42 (12), 1899–1901.

Griffioen, J., 2017. Enhanced weathering of olivine in seawater: The efficiency as revealed by thermodynamic scenario analysis. *Sci. Total Environ.* 575, 536–544.

Gunkel-Grillon, P., Laporte-Magoni, C., Lemestre, M., Bazire, N., 2014. Toxic chromium release from nickel mining sediments in surface waters, New Caledonia. *Environ. Chem. Lett.* 12 (4), 511–516.

Guo, J.A., Strzpek, R., Willis, A., Ferderer, A., Bach, L.T., 2022. Investigating the effect of nickel concentration on phytoplankton growth to assess potential side-effects of ocean alkalinity enhancement. *Biogeosciences* 19 (15), 3683–3697.

Hangx, S.J., Spiers, C.J., 2009. Coastal spreading of olivine to control atmospheric CO₂ concentrations: A critical analysis of viability. *Int. J. Greenh. Gas Control.* 3 (6), 757–767.

Hartmann, J., West, A.J., Renforth, P., Köhler, P., De La Rocha, C.L., Wolf-Gladrow, D.A., Dürr, H.H., Scheffran, J., 2013. Enhanced chemical weathering as a geoengineering strategy to reduce atmospheric carbon dioxide, supply nutrients, and mitigate ocean acidification. *Rev. Geophys.* 51 (2), 113–149.

Hauk, J., Köhler, P., Wolf-Gladrow, D., Völker, C., 2016. Iron fertilisation and century-scale effects of open ocean dissolution of olivine in a simulated CO₂ removal experiment. *Environ. Res. Lett.* 11 (2), 024007.

Hem, J.D., 1985. Study and Interpretation of the Chemical Characteristics of Natural Water, third ed. Department of the Interior, US Geological Survey, Alexandria.

Hofmann, A., Middelburg, J., Soetaert, K., Meysman, F., 2009. pH modelling in aquatic systems with time-variable acid-base dissociation constants applied to the turbid, tidal Scheldt estuary. *Biogeosciences* 6 (8), 1539–1561.

Hofmann, A.F., Soetaert, K., Middelburg, J.J., Meysman, F.J., 2010. AquaEnv: An aquatic acid-base modelling environment in R. *Aquat. Geochem.* 16 (4), 507–546.

Ivarsson, M., Broman, C., Holm, N.G., 2011. Chromite oxidation by manganese oxides in subseafloor basalts and the presence of putative fossilized microorganisms. *Geochem. Trans.* 12 (1), 1–10.

Jung, S., Jung, H., Austrheim, H., 2020. Microstructural evolution of amphibole peridotites in Åheim, Norway, and the implications for seismic anisotropy in the mantle wedge. *Minerals* 10 (4), 345.

Jung, S., Yamamoto, T., Ando, J.-I., Jung, H., 2021. Dislocation creep of olivine and amphibole in amphibole peridotites from Åheim, Norway. *Minerals* 11 (9), 1018.

Kanakalakshmi, A., Janaki, V., Shanthi, K., Kamala-Kannan, S., 2017. Biosynthesis of Cr (III) nanoparticles from electroplating wastewater using chromium-resistant *Bacillus subtilis* and its cytotoxicity and antibacterial activity. *Artif. Cells Nanomed. Biotechnol.* 45 (7), 1304–1309.

Kleiv, R.A., Thornhill, M., 2004. Adsorptive retention of copper from acidic mine water at the disused sulphide mine at Løkken, central Norway—initial experiments using olivine. *Miner. Eng.* 17 (2), 195–203.

Köhler, P., Hartmann, J., Wolf-Gladrow, D.A., 2010. Geoengineering potential of artificially enhanced silicate weathering of olivine. *Proc. Natl. Acad. Sci.* 107 (47), 20228–20233.

- Köhler, P., Abrams, J.F., Völker, C., Hauck, J., Wolf-Gladrow, D.A., 2013. Geoengineering impact of open ocean dissolution of olivine on atmospheric CO₂, surface ocean pH and marine biology. *Environ. Res. Lett.* 8 (1), 014009.
- Kuss, J., Schneider, B., 2004. Chemical enhancement of the CO₂ gas exchange at a smooth seawater surface. *Mar. Chem.* 91 (1–4), 165–174.
- Lafay, R., Montes-Hernandez, G., Renard, F., Vonlanthen, P., 2018. Intracrystalline reaction-induced cracking in olivine evidenced by hydration and carbonation experiments. *Minerals* 8 (9), 412.
- Luce, R.W., Bartlett, R.W., Parks, G.A., 1972. Dissolution kinetics of magnesium silicates. *Geochim. Cosmochim. Acta* 36 (1), 35–50.
- Lynn, K.J., Shea, T., Garcia, M.O., 2017. Nickel variability in Hawaiian olivine: Evaluating the relative contributions from mantle and crustal processes. *Am. Mineral.* 102 (3), 507–518.
- Madhavaraju, J., Armstrong-Altrin, J.S., James, R.A., Hussain, S., 2021. Palaeoenvironment and provenance signatures inferred from quartz grain surface features: A case study from Huatabampo and Altata beaches, Gulf of California, Mexico. *J. S. Am. Earth Sci.* 111, 103441.
- Maher, K., 2010. The dependence of chemical weathering rates on fluid residence time. *Earth Planet. Sci. Lett.* 294 (1–2), 101–110.
- Maher, K., Johnson, N.C., Jackson, A., Lammers, L.N., Torchinsky, A.B., Weaver, K.L., Bird, D.K., Brown Jr, G.E., 2016. A spatially resolved surface kinetic model for forsterite dissolution. *Geochim. Cosmochim. Acta* 174, 313–334.
- Marion, G., Millero, F., Feistel, R., 2009. Precipitation of solid phase calcium carbonates and their effect on application of seawater S A-T-P models. *Ocean Sci.* 5 (3), 285–291.
- McClenaghan, N.W., Schindler, M., 2022. Release of chromite nanoparticles and their alteration in the presence of Mn-oxides. *Am. Mineral.* 107 (4), 642–653.
- Meysman, F.J., Montserrat, F., 2017. Negative CO₂ emissions via enhanced silicate weathering in coastal environments. *Biol. Lett.* 13 (4), 20160905.
- Millero, F.J., 1998. Solubility of Fe (III) in seawater. *Earth Planet. Sci. Lett.* 154 (1–4), 323–329.
- Minx, J.C., Lamb, W.F., Callaghan, M.W., Fuss, S., Hilaire, J., Creutzig, F., Amann, T., Beringer, T., de Oliveira Garcia, W., Hartmann, J., 2018. Negative emissions—Part 1: Research landscape and synthesis. *Environ. Res. Lett.* 13 (6), 063001.
- Montserrat, F., Renforth, P., Hartmann, J., Leermakers, M., Knops, P., Meysman, F.J., 2017. Olivine dissolution in seawater: implications for CO₂ sequestration through enhanced weathering in coastal environments. *Environ. Sci. Tech.* 51 (7), 3960–3972.
- Moosdorf, N., Renforth, P., Hartmann, J., 2014. Carbon dioxide efficiency of terrestrial enhanced weathering. *Environ. Sci. Tech.* 48 (9), 4809–4816.
- Moras, C.A., Bach, L.T., Cyronak, T., Joannes-Boyau, R., Schulz, K.G., 2022. Ocean alkalinity enhancement—avoiding runaway CaCO₃ precipitation during quick and hydrated lime dissolution. *Biogeosciences* 19 (15), 3537–3557.
- Morse, J.W., Arvidson, R.S., Lüttge, A., 2007. Calcium carbonate formation and dissolution. *Chem. Rev.* 107 (2), 342–381.
- Moum, J.N., 2021. Variations in ocean mixing from seconds to years. *Ann. Rev. Mar. Sci.* 13, 201–226.
- Muysen, B.T., Brix, K., DeForest, D., Janssen, C., 2004. Nickel essentiality and homeostasis in aquatic organisms. *Environ. Rev.* 12 (2), 113–131.
- Oelkers, E.H., Declercq, J., Saldi, G.D., Gislason, S.R., Schott, J., 2018. Olivine dissolution rates: A critical review. *Chem. Geol.* 500, 1–19.
- Pan, Y., Li, Y., Ma, Q., He, H., Wang, S., Sun, Z., Cai, W.-J., Dong, B., Di, Y., Fu, W., 2021. The role of Mg²⁺ in inhibiting CaCO₃ precipitation from seawater. *Mar. Chem.* 237, 104036.
- Parkhurst, D.L., Appelo, C., 2013. Description of input and examples for PHREEQC version 3—a computer program for speciation, batch-reaction, one-dimensional transport, and inverse geochemical calculations. *US Geol. Surv. Tech. Methods* 6 (A43), 497.
- Penman, D.E., Rugenstein, J.K.C., Ibarra, D.E., Winnick, M.J., 2020. Silicate weathering as a feedback and forcing in Earth's climate and carbon cycle. *Earth Sci. Rev.* 209, 103298.
- Pokrovsky, O.S., Schott, J., 2000a. Forsterite surface composition in aqueous solutions: a combined potentiometric, electrokinetic, and spectroscopic approach. *Geochim. Cosmochim. Acta* 64 (19), 3299–3312.
- Pokrovsky, O.S., Schott, J., 2000b. Kinetics and mechanism of forsterite dissolution at 25 °C and pH from 1 to 12. *Geochim. Cosmochim. Acta* 64 (19), 3313–3325.
- Precht, E., Huettel, M., 2003. Advective pore-water exchange driven by surface gravity waves and its ecological implications. *Limnol. Oceanogr.* 48 (4), 1674–1684.
- Pruszk, Z., Zeidler, R.B., 1994. Sediment transport in various time scales. In: Edge, B.L. (Eds.), *Coastal Engineering 1994, Japan*, pp. 2513–2526.
- R Core Team, 2022. *R: A Language and Environment for Statistical Computing*. R Foundation for Statistical Computing, Vienna, Austria. <http://www.R-project.org/>.
- Ren, H., Hu, Y., Liu, J., Zhang, Z., Mou, L., Pan, Y., Zheng, Q., Li, G., Jiao, N., 2021. Response of a coastal microbial community to olivine addition in the Muping Marine Ranch, Yantai. *Front. Microbiol.* 12, 805361.
- Rigopoulos, I., Harrison, A.L., Delimitis, A., Ioannou, I., Efstathiou, A.M., Kyratsi, T., Oelkers, E.H., 2018. Carbon sequestration via enhanced weathering of peridotites and basalts in seawater. *Appl. Geochem.* 91, 197–207.
- Rimstidt, J.D., Brantley, S.L., Olsen, A.A., 2012. Systematic review of forsterite dissolution rate data. *Geochim. Cosmochim. Acta* 99, 159–178.
- Santos, I.R., Eyre, B.D., Huettel, M., 2012. The driving forces of porewater and groundwater flow in permeable coastal sediments: A review. *Estuar. Coast. Shelf Sci.* 98, 1–15.
- Santos, R.M., Van Audenaerde, A., Chiang, Y.W., Iacobescu, R.L., Knops, P., Van Gerven, T., 2015. Nickel extraction from olivine: effect of carbonation pre-treatment. *Metals* 5 (3), 1620–1644.
- Sarmiento, J.L., 2013. *Ocean Biogeochemical Dynamics*. Princeton University Press, Princeton.
- Schilling, R.D., De Boer, P.L., 2011. Rolling stones; fast weathering of olivine in shallow seas for cost-effective CO₂ capture and mitigation of global warming and ocean acidification. *Earth Syst. Dyn. Discuss.* 2, 551–568.
- Schilling, R.D., Krijgsman, P., 2006. Enhanced weathering: an effective and cheap tool to sequester CO₂. *Clim. Change* 74 (1), 349–354.
- Seyama, H., Soma, M., Tanaka, A., 1996. Surface characterization of acid-leached olivines by X-ray photoelectron spectroscopy. *Chem. Geol.* 129 (3–4), 209–216.
- Sun, W., Jayaraman, S., Chen, W., Persson, K.A., Ceder, G., 2015. Nucleation of metastable aragonite CaCO₃ in seawater. *PNAS* 112 (11), 3199–3204.
- Sun, M., Wu, W., Ji, X., Wang, X., Qu, S., 2019. Silicate weathering rate and its controlling factors: A study from small granitic watersheds in the Jiuhua Mountains. *Chem. Geol.* 504, 253–266.
- Taylor, L.L., Quirk, J., Thorley, R.M., Kharcha, P.A., Hansen, J., Ridgwell, A., Lomas, M. R., Banwart, S.A., Beerling, D.J., 2016. Enhanced weathering strategies for stabilizing climate and averting ocean acidification. *Nat. Clim. Chang.* 6 (4), 402–406.
- Tebo, B.M., Bargar, J.R., Clement, B.G., Dick, G.J., Murray, K.J., Parker, D., Verity, R., Webb, S.M., 2004. Biogenic manganese oxides: properties and mechanisms of formation. *Annu. Rev. Earth Planet. Sci.* 32, 287–328.
- Thompson, J.F., Barnes, S.J., Duke, J.M., 1984. The distribution of nickel and iron between olivine and magmatic sulfides in some natural assemblages. *Can. Mineral.* 22 (1), 55–66.
- Toffoli, A., Bitner-Gregersen, E.M., 2017. Types of ocean surface waves, wave classification. *Encyclopedia Maritime Offshore Eng.* 1–8.
- UNFCCC, 2015. *Paris agreement. Paper presented at the Report of the Conference of the Parties to the United Nations Framework Convention on Climate Change (21st Session, 2015: Paris)*.
- Varadachari, C., Barman, A.K., Ghosh, K., 1994. Weathering of silicate minerals by organic acids II. Nature of residual products. *Geoderma* 61 (3–4), 251–268.
- Wang, X., Wang, J., Zhang, J., 2012. Comparisons of three methods for organic and inorganic carbon in calcareous soils of northwestern China. *PLoS One* 7 (8), e44334.
- Wogelius, R.A., Walther, J.V., 1992. Olivine dissolution kinetics at near-surface conditions. *Chem. Geol.* 97 (1–2), 101–112.
- Yu, F., Hunt, A.G., 2017. Damkohler number input to transport-limited chemical weathering calculations. *ACS Earth Space Chem.* 1 (1), 30–38.